ASSESSING THE MECHANISMS GOVERNING THE DAYTIME EVOLUTION OF MARINE STRATOCUMULUS USING LARGE-EDDY SIMULATION

BY

Lucas A. McMichael

Submitted to the graduate degree program in Geography and Atmospheric Sciences and the Graduate Faculty of the University of Kansas in partial fulfillment of the requirements for the degree of Master of Science.

Chair: David B. Mechem

David A. Rahn

David A. Braaten

Date Defended: 6 December 2017

The thesis committee for Lucas McMichael

certifies that this is the approved version of the following thesis:

ASSESSING THE MECHANISMS GOVERNING THE DAYTIME EVOLUTION OF MARINE STRATOCUMULUS USING LARGE-EDDY SIMULATION

Chair: David B. Mechem

Date Defended: 6 December 2017

Abstract

The individual mechanisms responsible for governing the evolution of afternoon cloud properties were explored for a case of thin stratocumulus off the coast of California by applying mixed-layer theory to Large-Eddy Simulation (LES) output. The development of a cloud-base tendency equation permitted the determination of the relative importance of mechanisms governing the evolution of boundary-layer liquid-water static energy (S_l) and total water mixing ratio (q_T). The Control simulation performed admirably in comparison to observed estimates of liquid water content, vertical velocity variance, and radiative fluxes sampled by the CIRPAS Twin Otter aircraft. The cloud response to various environmental forcing scenarios was investigated through a suite of sensitivity tests, including variations in subsidence velocity, temperature/moisture tendencies, surface fluxes, wind shear near the inversion, and radiative forcing. In the Control simulation, rising cloud-base tendencies were related to entrainment warming and drying and shortwave absorption, while lowering cloud-base tendencies were associated with longwave cooling. Although there was substantial solar heating during the afternoon, the entrainment fluxes remained active throughout the analysis period. A reversal of cloud-base tendency was often observed in the simulations, as the reduction in shortwave warming later in the afternoon allowed for the recovery of the cloud. The evolution of cloud-base tendency is found to be insensitive to the net radiative flux divergence for most of the simulations (LWP ranging from ~10-50 g m^{-2}). Error analysis suggests our method of entrainment flux calculation could be improved by a more complete understanding of entrainment layer physics.

Acknowledgements

I would like to thank my advisor, Dr. David Mechem, for countless hours of discussion and guidance. I would also like to thank Dr. David Rahn and Dr. David Braaten for taking the time to serve on my committee and providing helpful feedback. Thank you to Dr. Qing Wang from the Naval Postgraduate School for providing aircraft observations and counsel regarding the incorporation of observations. Thank you to Dr. Shouping Wang from the Naval Research Laboratory for supplying COAMPS support and invaluable input on research methods. I would like to thank the Office of Naval Research for funding my research with award number N00014-11-1-0518. Thank you to all of the graduate students that I have had the pleasure of meeting that made this experience thoroughly enjoyable as we grew as scientists and friends. Thank you to all of the faculty in the Department of Geography and Atmospheric Sciences for creating an environment that is conducive for research. A big thank you to my parents, Glenn and Julie, and siblings, Matt and Sarah, for continuing to support my educational career and always being available for emotional support. I would like to thank my family and friends near and far for the continued relationships that make life fulfilling.

CHAPTER 1

Introduction

Stratocumulus clouds are ubiquitous in the lower troposphere and are the dominant cloud type on Earth, covering approximately one-third of the ocean surface on average (Klein and Hartmann 1993; Warren et al. 1986, 1988). Stratocumulus clouds typically coincide with regions of statically stable lower-tropospheric conditions, which commonly occur over cold oceans and in regions of large-scale subsidence such as the descending branches of the Hadley and Walker circulations (Klein and Hartmann 1993). Because of the combination of large areal cloud coverage and high albedo (Chen et al. 2000), marine stratocumulus play an important role in the global radiation budget. Minor differences in cloud thickness and cover can have major implications on radiation budgets, comparable to those caused by increasing greenhouse gas concentrations (Hartman and Short 1980). For example, Randall et al. (1984) estimated that a 4% increase in the Earth's area covered by marine stratocumulus would provide a negative feedback strong enough to counteract a doubling in CO_2 concentrations. Understanding the processes governing the evolution of stratocumulus is crucial in correctly modeling the global radiation budget.

The diurnal cycle of stratocumulus clouds is well documented, with a typical peak in coverage and thickness during the early morning hours (Rozendaal et al. 1995). Maximum drizzle production also coincides with the early morning peak in stratocumulus thickness (Leon et al. 2008; Comstock et al. 2004; Sears-Collins et al. 2006; Burleyson et al. 2013). Burleyson and Yuter (2015) determined that the diurnal cycle of cloud fraction was dependent on the region being observed, with the NE Pacific showing the lowest amplitude variability and slowest rates of dissipation, in contrast to the SE Pacific and SE Atlantic. The earliest cloud break-up times

normally occur near the edges of the stratocumulus deck and correspond to lower values of cloud fraction (Burleyson and Yuter 2015). The fastest rates of dissipation typically occur around 1200 LT and decrease until ~1500-1600 LT, when shortwave fluxes decrease (Burleyson and Yuter 2015).

Similar to nighttime conditions, daytime stratocumulus dynamics remain convectively driven by longwave cooling at cloud-top, but longwave cooling is supplemented by solar absorption (Wood 2012; Caldwell et al. 2005), which is dependent upon cloud optical depth, droplet size, and the solar zenith angle (Stephens 1978). By limiting negative buoyancy production near cloud-top, solar absorption reduces entrainment rates and evaporative cooling potential through a decrease in boundary-layer turbulent kinetic energy (TKE) (Bretherton and Wyant 1997). In the absence of stronger turbulent eddies, sub-cloud moisture is unable to be transported into the cloud-layer, which as a result warms and dries with respect to the sub-cloud layer. This asymmetry is reflected in downward moving parcels reaching their lifted-condensation levels (LCLs) at a higher level than the LCL for surface-based updrafts (Stevens et al. 1998; Wood 2012; de Roode et al. 2016). This situation leads to stabilization, associated negative buoyancy fluxes near the cloud-base, and a decoupling of the boundary-layer into distinct cloud and sub-cloud layer circulations (Nicholls and Leighton 1986). In thicker clouds, drizzle can also promote decoupling by evaporating in the sub-cloud layer and stabilizing the boundary-layer. The decoupled, conditionally unstable (as opposed to well-mixed) boundary-layer can occasionally support isolated cumulus development (Stevens et al. 1998). These cumulus clouds are associated with vigorous updrafts that may generate enhanced entrainment rates and a gradual dissipation of the overlying stratocumulus (de Roode et al. 2016). There have been relatively few attempts to comprehensively examine daytime tendencies in cloud properties

under a wide range of environmental forcing scenarios to explore the dominant mechanisms responsible for cloud evolution.

Large-eddy simulation (LES) explicitly resolves the larger boundary-layer scale eddies responsible for a majority of the energy and moisture transport (Lewellen and Lewellen 1998) in the boundary-layer and is a valuable tool for testing hypotheses regarding shallow clouds. Stratocumulus transitioning from solid to broken cloud regimes in the daytime hours are particularly sensitive to perturbations, and model representations of stratocumulus depend greatly on an accurate portrayal of cloud-top entrainment (Stevens et al. 2005). Stevens et al. (2005) stressed the importance of the rather uncertain aspects of LES involved in dictating the entrainment rate, such as sub-grid scale mixing and numerical diffusion, which may ultimately determine the degree of radiative forcing and evaporative cooling experienced by the cloud system. Despite the aforementioned uncertainties, Sandu and Stevens (2011) were able to reproduce the main features of non-steady state stratocumulus-to-cumulus (SCT) transitions in comparison with observations, which is a testament of the utility of LES in modeling transient cloud systems. Ghonima et al. (2016) used a combination of LES and mixed-layer models (MLMs) and found that the controlling factors dictating stratocumulus lifetime over coastal land regions were the cloud-top entrainment rate, the Bowen ratio at the surface, and the strength of cold air advection induced by the daytime sea-breeze circulation. However, in our case, the modulating daytime stratocumulus processes over the cool ocean surface are fundamentally different with a lack of strong sensible heat fluxes to promote efficient boundary-layer coupling (Ghonima et al. 2016).

In spite of the previously discussed mechanisms leading to cloud thinning during the daylight hours, stratocumulus clouds are generally resilient to perturbations, owing to the cloud-

radiation-turbulent-entrainment feedback (Zhu et al. 2005). This feedback arises from the relationship between cloud thickness and entrainment rate, with thicker clouds promoting stronger entrainment of warm, dry air through stronger evaporative cooling potential and increased TKE, whereas thinner clouds reduce entrainment as a result of having a lower liquid water content (Wood 2012). Additionally, Sandu et al. (2008) found that in cases where afternoon stratocumulus drizzle was not strong enough to reach the surface, evaporation below the cloud-base resulted in destabilization with respect to the surface. The destabilization from the evaporation of drizzle acts to promote deeper-layer mixing and dampens the susceptibility to decoupling that would normally be anticipated given the shortwave absorption in the cloud-layer (Sandu et al. 2008).

The cloud-top entrainment instability (CTEI) criterion was formulated to provide a metric for rapid cloud break-up based on the strength of energy and moisture gradients and the resulting evaporative potential (Randall 1980; Deardoff 1980); however, it is well documented that stratocumulus can persist under conditions that promote rapid break-up under CTEI assumptions (Stevens et al. 2003). More recently, it has been found that a monotonic decrease in liquid water path (LWP) coincided with an attendant increase in the CTEI criterion (Yamaguchi and Randall 2008; Noda et al. 2013). Noda et al. (2013) found this relationship to be associated with the state of the entrainment interfacial layer, as cloud-top mixing inhibits negative buoyancy production through cooling and decreased evaporative potential of the air drawn into the cloud layer. The dependence on factors other than the strength of energy and moisture gradients suggests the need for other mechanisms to be considered and more robust predictors of afternoon cloud dissipation/evolution to be developed. Although the CTEI criterion has been found lacking, it

attempts to address an important question: What are the main drivers promoting changes in cloud properties under varying environmental forcings?

Variations in subsidence velocity, radiative flux divergence, surface fluxes, inversion structure, free-tropospheric conditions, and moisture/temperature advection occur across a wide range of temporal and spatial scales. The interconnectedness of the forcing mechanisms introduces a considerable amount of uncertainty when attempting to disentangle the relative importance of the individual mechanisms of dissipation (Caldwell et al. 2005). Contrary to previous studies where MLMs have been used in comparison with LES output (Ghonima et al. 2016), this research aims to cast LES output into a MLM framework. The advantage of the MLM budget approach lies in its ability to address a specific question: Which of the possible mechanisms are most responsible for governing the evolution of the cloud properties? This question is explored through a series of model sensitivity experiments and a novel application of mixed-layer theory to model output. In Chapter 2, the LES and control configuration are discussed for a thin afternoon stratocumulus case off the coast of California. The formulation of the MLM closely follows the methods of Ghonima et al. (2016) and Wood (2007) and is included in Chapter 2. Detailed discussions of sensitivity-test results and MLM budget analysis and uncertainties are presented in Chapter 3. Ultimately, knowledge of mechanisms that govern cloud evolution should lead to better prediction of afternoon stratocumulus and more accurate representation of these clouds in numerical weather prediction (NWP) models, through the implementation of more representative parameterizations and cloud dissipation metrics.

CHAPTER 2

Methodology

2.1. UPPEF RF01 Observations

All simulations are based on observations collected during the first research flight (RF01) of the Unified Physical Parameterization for Extended Forecast (UPPEF) field campaign on 31 August 2012. Synoptic conditions supported coastal stratocumulus development during the overnight hours with the presence of a substantial stable layer (inversion strength of ~10 K) near 900 m and considerable cloud-top cooling. A near neutrally-tilted 500-mb trough was propagating eastward producing weak mid-level height falls and by 0000 UTC was aligned with the northern California coast (Fig. 1). Near the surface, modest pressure rises occurred throughout the afternoon (attendant 925-mb height falls) with winds generally out of the north/northwest (Fig. 1). Overall, large-scale forcing was limited, with the more significant large-scale motions confined to the Pacific Northwest/British Columbia vicinity.

The CIRPAS (Center for Interdisciplinary Remotely-Piloted Aircraft Studies) Twin Otter aircraft departed from the Marina Airport at approximately 1900 UTC (local noon) and sampled the coastal environment during its 5-hour long flight. The Twin Otter paid special interest to the sharp clear/cloud boundary in the stratocumulus, which resided on the cool side of a strong sea surface temperature (SST) gradient. The SST gradient was oriented from northwest to southeast paralleling the California coast and separated the western periphery of the nearly homogeneous, small horizontal-cell structure (~2 km) stratocumulus from a narrow corridor of clear air (Fig. 2). The aforementioned stratocumulus deck was approximately 75 nautical miles in width and extended from Cape Mendocino to Santa Barbara, with a relatively shallow vertical depth generally ranging from 100-300 m. West of 125˚W featured deep stratocumulus with cell sizes

on the order of 50 km, but this western stratocumulus regime was not sampled by the aircraft (Wang et al. 2014). After 2000 UTC, dissipation of the coastal stratocumulus deck ensued during

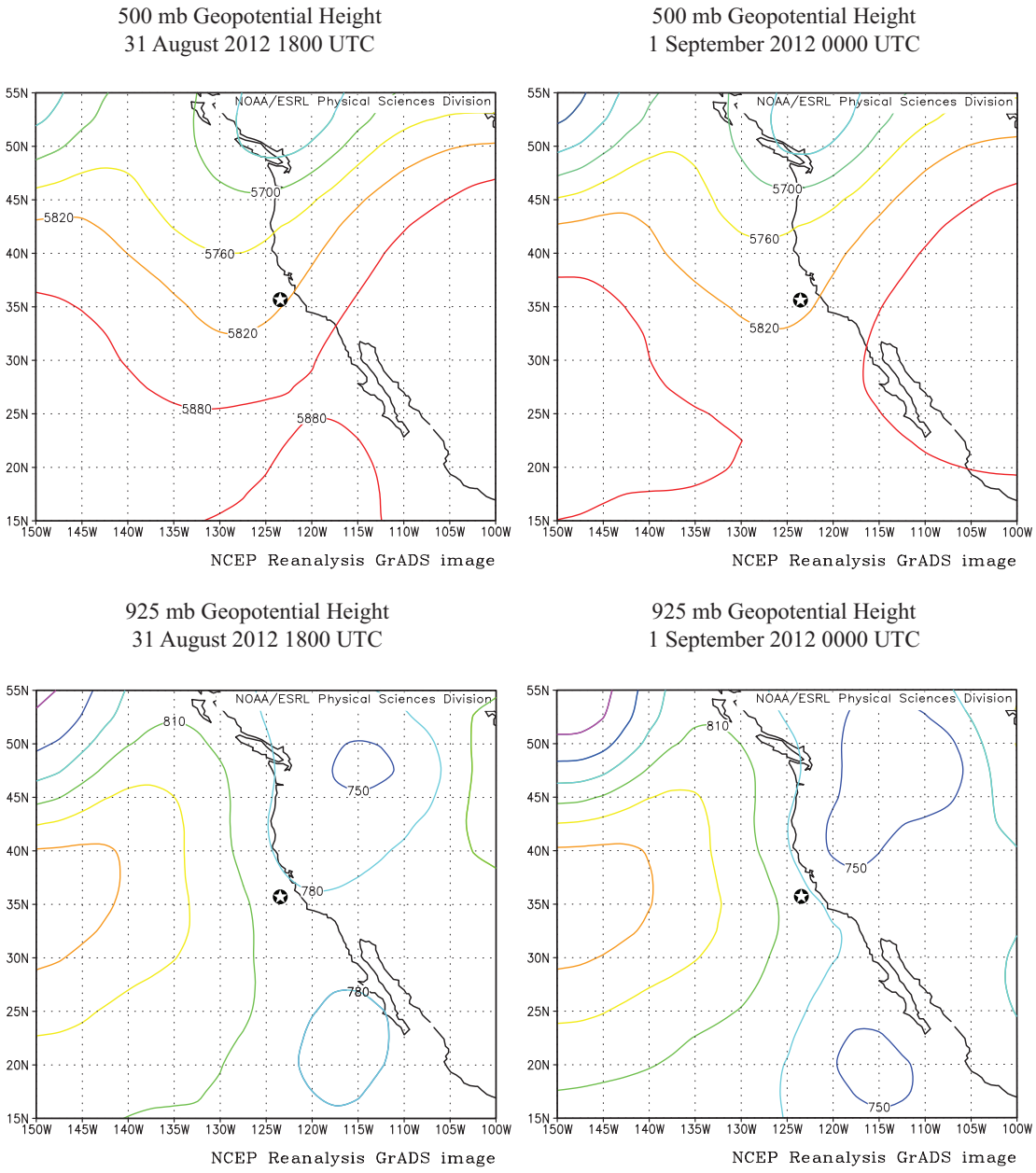

Fig. 1. Top Row: NCAR reanalysis of 500 mb geopotential heights for 31 August 2012 and 1 September 2012. Bottom Row: 925 mb geopotential heights. *Image provided by Physical Sciences Division, Earth System Research Laboratory, NOAA, Boulder, Colorado, from their Web site at http://www.esrl.noaa.gov/psd/.*

the next several hours, extending from Monterey Bay to near Point Conception, with portions of the cloud deck remaining intact to the north and south of these locations, respectively. Figure 2 displays hourly visible satellite imagery analysis from GOES-15 and a depiction of a larger version of our Lagrangian model domain (moving with the mean flow), which suggests cloud recovery after 2300 UTC as insolation decreases.

The CIRPAS Twin Otter aircraft was equipped with a large suite of instruments. The aircraft gathered horizontal and vertical velocities at a frequency of 40 Hz, absolute humidity using a modified Campbell Scientific fast krypton hygrometer (KH20) and LI-COR 7500 gas analyzer, bulk liquid water content measured with a PVM-100A probe, and ambient temperatures using a Rosemount total temperature sensor, as well as many other particle and drop size distribution/concentration measurements not examined in this research (Wang et al. 2014). The aircraft also gathered downwelling and upwelling solar irradiance (Kipp and Zonen CM-22 pyranometers), along with upwelling infrared irradiance (Kipp and Zonen CG4 pyrgeometers). The downwelling infrared pyrgeometer was inoperative. All radiation measurements were gathered at a frequency of 1 Hz (Wang et al. 2014).

The focal point of the UPPEFF RF01 was to investigate the differences in surface fluxes between the clear and cloudy regions, separated in RF01 by the SST gradient mentioned previously. Much of the flight duration was spent attempting to measure surface/near-surface fluxes and the low-level turbulent structure in proximity to the clear/cloud boundary. Therefore, comparatively little emphasis was given to level-legs in the cloud layer and full soundings through the depth of the cloud layer. For this reason, we are somewhat limited in terms of observations in a Lagrangian model framework of the evolution of cloud properties over the

afternoon. Nevertheless, we strive to incorporate all available measurements to constrain and validate model behavior.

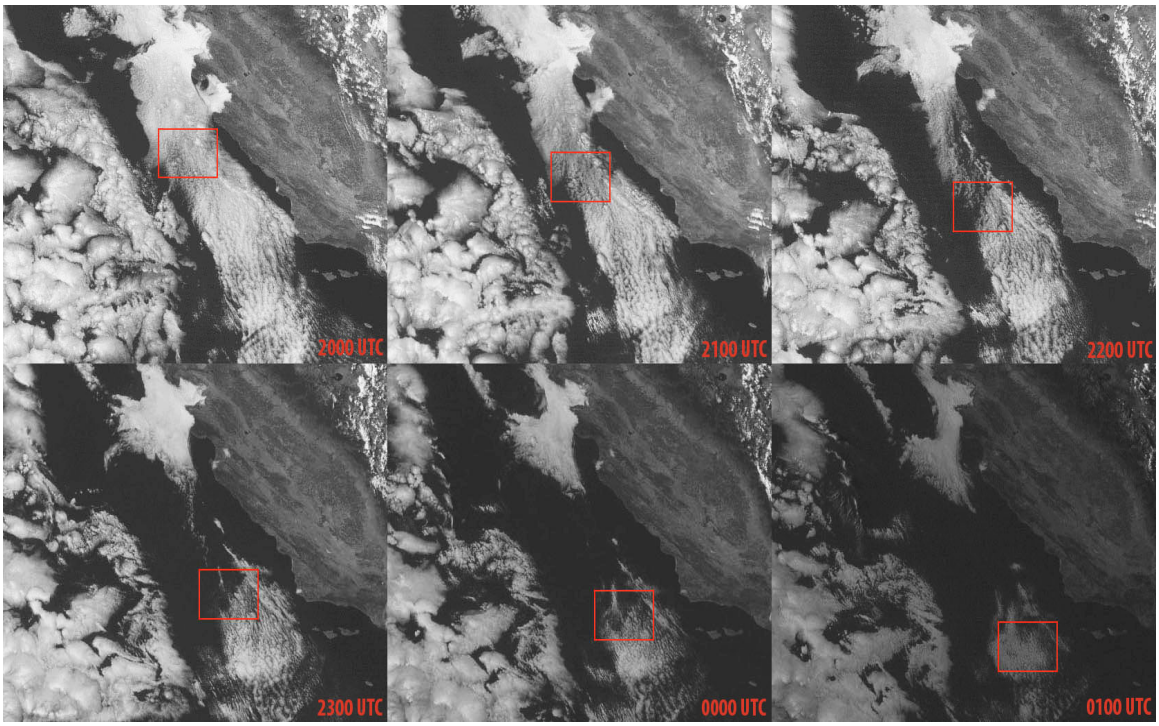

Fig. 2. GOES-15 visible satellite imagery at hourly intervals (2000 UTC – 0100 UTC) on August 31st, 2012. Red box denotes the Lagrangian analysis domain moving at a constant velocity of 13.5 m s^{-1} out of the NNW (335˚)

2.2. Model Configuration

Simulations were performed using the System for Atmospheric Modeling (SAM), version 6.10.6 (Khairoutdinov and Randall 2003). SAM is a non-hydrostatic model that employs the anelastic approximation, which filters acoustic waves. The model was run in traditional LES mode over the ocean surface, assuming horizontally homogeneous surface fluxes across the entire domain. Surface sensible and latent heat fluxes were prescribed using fluxes measured by the Twin Otter, while surface momentum fluxes were computed according to Monin-Obukhov

Similarity Theory, with a surface roughness height of 0.1 cm (Monin and Obukhov 1954). The model employs thermodynamic variables of liquid water static energy (S_l) and total water mixing ratio (q_T), which are conserved for moist-adiabatic processes. A 5th-order advection scheme (ULTIMATE-MACHO; Yamaguchi et al. 2011) was implemented to limit numerical diffusion and the associated damping of turbulent kinetic energy (TKE). Numerical solutions to the partial differential equations for momentum were solved using the 3rd-order Adams-Bashforth time-differencing method. The CAM3 radiation package (Collins et al. 2006) was used for longwave and shortwave radiative fluxes for every model time step (2s) with a diurnally varying zenith angle. The sub-grid scale turbulence scheme uses a prognostic 1.5-order turbulent kinetic energy (TKE) closure developed by Deardoff (1980), which predicts the TKE using shear and stability profiles and diagnoses eddy diffusivity and dissipation.

Detailed representations of precipitation processes are of little significance in this essentially non-precipitating event, so single-moment (hydrometeor mixing ratio) bulk microphysics were used to increase computational efficiency. This simple microphysics parameterization assumes saturation adjustment to diagnose liquid water content and partitions hydrometeors into precipitating and non-precipitating classes (Kessler 1969). The model does not account for cloud droplet sedimentation, which has been found to reduce excessive entrainment (Ackerman et al. 2004; Bretherton et al. 2007), but we speculate this mechanism to be less important for low liquid water content clouds (and hence small droplets) investigated in our study. A vertically refined grid of 5 m in the 600-1000 m layer, similar to that used by Caldwell and Bretherton (2009), is used to minimize computational cost and attempt to accurately simulate cloud-top entrainment (Fig. 3). The vertical grid is approximately 21 km (168 grid levels) in depth in order to sufficiently model downwelling radiative fluxes in the

boundary-layer. A simulation using a 5-m vertical grid spacing throughout the entire depth from 0-1500 m was nearly indistinguishable from the stretched grid run, augmenting confidence in our stretched vertical grid structure. Our configuration, along with several other studies, has shown that entrainment is rather unresponsive to horizontal grid spacing (Lewellen and Lewellen 1998; Stevens et al. 1999), so a fairly coarse horizontal grid of 35 m was employed. The model consists of 128×128 grid points in the horizontal, equating to a 4.48×4.48 km^2 horizontal grid initially centered on (35.9˚N, 123.4˚W). Boundary conditions are doubly periodic and the vertical damping of waves at the top 30% of the domain was accomplished by a Rayleigh sponge layer. All simulations are run for 6 hours, and statistics are computed using 30-minute averages.

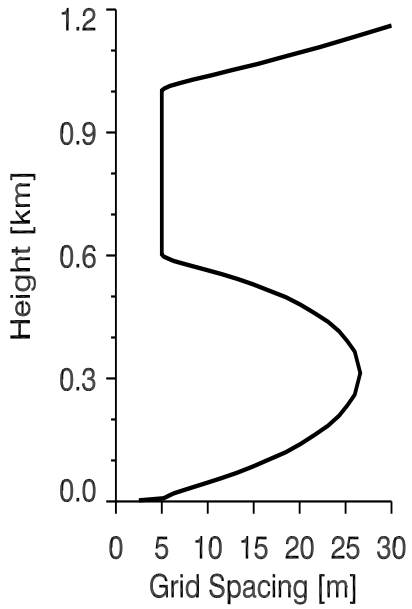

Fig. 3. Bottom 1.2 km of vertically stretched grid with refined grid spacing near the surface and the inversion layer (600 – 1000 m)

2.3. Model Initialization and Optimal Spin-up Procedure

Initialization soundings below 1200 m were derived from the 7-minute aircraft descent from 2113-2120 UTC, which sampled the thin cloud layer on the cool side of a strong SST gradient (the warm side was predominantly cloud-free). Aircraft observations indicate initial stratification in the total water mixing ratio profile, with a surface value of 8.75 g kg^{-1} and an inversion base value of 7.25 g kg^{-1}. The observed liquid water potential temperature profile was nearly constant over the boundary layer, with an inversion depth of approximately 25 m and a cloud-top jump of 9.5 K separating the boundary layer from the free troposphere. Vertical profiles of horizontal velocities revealed minimal shear in the *u*-component and evidence of a moderate coastal jet in the *v*-component with a strong northerly flow (7-10 m s^{-1}) in the boundary layer. Smoothed aircraft-derived initialization profiles of liquid potential temperature, total water mixing ratio, and horizontal velocities are shown in Figure 4. Atmospheric moisture and temperature profiles above 1200 m were estimated using a blend of the 1200/0000 UTC Oakland soundings. Synoptic forcing was weak and the atmosphere nearly barotropic, so the winds above 1200 m were assumed to be constant and out of the NNW at 6.4 m s^{-1}. Surface fluxes were prescribed according to aircraft observations, with sensible and latent heat fluxes of 0.00 and 4.45 W m^{-2}, respectively.

All simulations assume a Lagrangian framework, justified by the minimal vertical shear in the lower atmosphere and weak horizontal moisture and temperature gradients, so large-scale advective tendencies are unnecessary. Estimates of large-scale vertical motion are based on the inner, 5-km nest of a doubly nested operational run of the Coupled Ocean-Atmosphere Mesoscale Prediction System (COAMPS; Hodur 1997) conducted in support of the field campaign. We simplified the COAMPS vertical motion profile to decrease linearly from 0 cm s^{-1}

at the surface to –1.0 cm s^{-1} at 900 m remaining constant up to a height of 6 km. Above 6 km, subsidence velocities decrease linearly to 0 cm s^{-1} by 10 km.

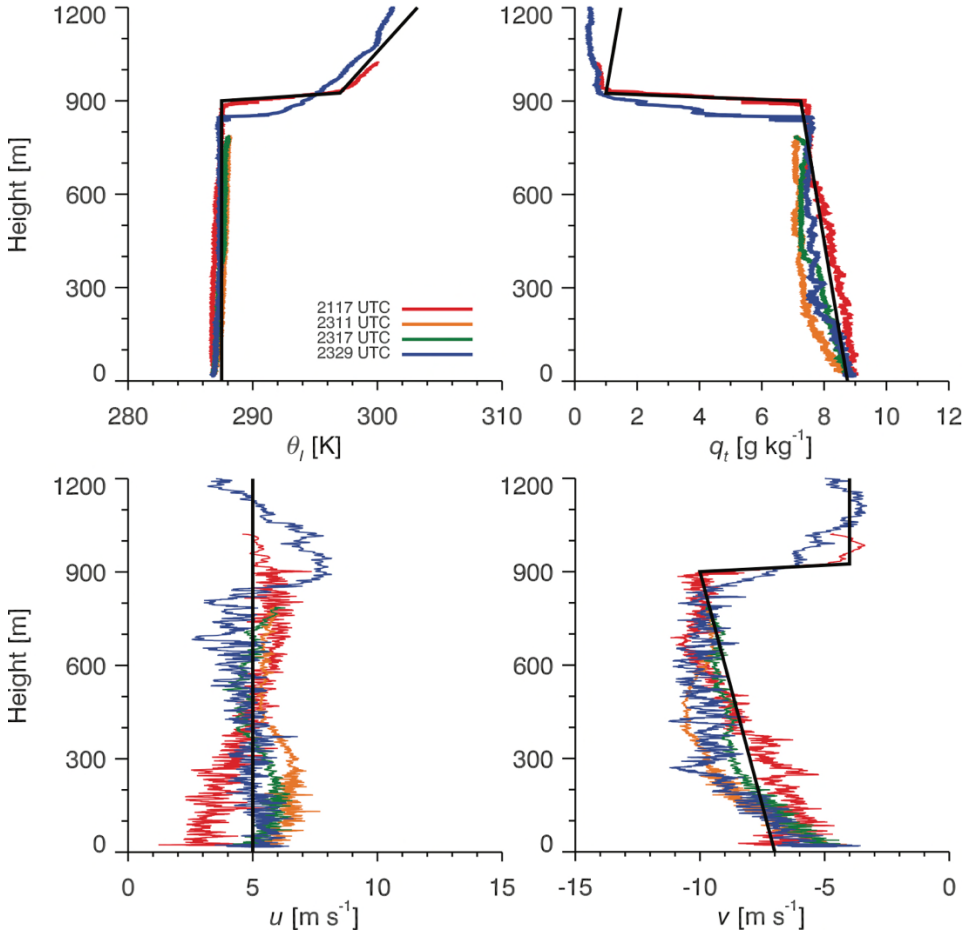

Fig. 4. Idealized profiles (black lines) used for model initialization with observed aircraft soundings in the vicinity of the primary aircraft sounding (2117 UTC) superimposed. Top Left: Liquid potential temperature Top Right: Total water mixing ratio Bottom Left: u-velocity component Bottom Right: v-velocity component

By the addition of random noise to the model initial conditions, the initial quiescent state is perturbed and turbulence develops. The time it takes this perturbed state to reach a dynamic equilibrium is referred to as the model spin-up time. This particular non-steady-state stratocumulus case presents several challenges since there is a significant dependence on time,

and the model solution must arrive at a post-spin-up state that represents observed thermodynamic and dynamic structures. In other words, by the time the spin-up process is complete, ideally, the thermodynamic and dynamic fields must be well-matched to our observations. Our SAM configuration has a spin-up time of roughly 1.25 hours. We attempted to find an optimal solution that evolved appropriately, according to aircraft and satellite observations of the case using various methods to slightly increase initial LWP, including cold air advection (to account for possible baroclinic aspects of the observational setup not well represented by our Lagrangian framework), reducing subsidence, employing only longwave radiation, and altering surface fluxes during the spin-up period. The optimal spin-up procedure is discussed in Chapter 3 and will hereafter be called the Control run.

2.4. Sensitivity Tests

All sensitivity tests incorporate the Control spin-up process, with large-scale forcing being applied after spin-up has completed and at a constant value for the remainder of simulation. Since the Control run atmospheric conditions above 1200 m were approximated from Oakland soundings (KOAK), additional simulations varying initial free-tropospheric temperature and moisture profiles were performed to determine the impact that variations in these profiles have on boundary-layer cloud behavior. Once we determined the LES configuration was performing satisfactorily, a substantial suite of sensitivity simulations was completed. In order to discover how thin stratocumulus responds to various forcing scenarios the simulations explore changes in large-scale subsidence, large-scale temperature/moisture tendencies, wind shear across the inversion, surface fluxes, and radiative forcing. Despite the Lagrangian frame of reference, large-scale temperature/moisture tendencies imply “advection” and emulate possible

weak baroclinic influences. Model output from sensitivity tests was used to assure model responses were reasonable according to known cloud/forcing relationships discussed in the literature, and to gain insights into how the modeled cloud evolves under wide ranges of environmental conditions using a mixed-layer budget approach detailed in Section 2.5. Descriptions of how forcings were applied are summarized here:

- Large-scale subsidence sensitivity was examined by applying a range of subsidence values from 0–1.5 cm s^{-1} in the 900-6000 m layer.
- Large-scale temperature tendency sensitivity was explored using both negative and positive temperature tendencies ranging from 0-2 K hr^{-1} in the 0-900 m layer.
- Large-scale moisture tendency sensitivity was investigated using negative and positive moisture tendencies ranging from 0-1 g kg^{-1} hr^{-1} in the 0-900 m layer.
- Surface flux sensitivity tests were performed using latent and sensible heat fluxes ranging from 100-150 W m^{-2}.
- Wind shear across the inversion sensitivity was studied using four different scenarios:

    1.) No shear, with flow invariable with height out of the northwest at 6.4 m s^{-1}.

    2.) Directional shear with southeasterly winds in the boundary layer (0-900 m) and northwesterly winds above 925 m, with both having a velocity magnitude of 6.4 m s^{-1}.

    3.) Speed shear that induced positive vorticity near the inversion, with a velocity magnitude of 6.4 m s^{-1} from 0-900 m and 12.8 m s^{-1} from 925-1500 m, thereafter it relaxed back to 6.4 m s^{-1}.

    4.) Speed shear that induced negative vorticity near the inversion, with a velocity magnitude of 12.8 m s^{-1} from 0-900 m and 6.4 m s^{-1} from 925 m and above.

- Radiative forcing sensitivity was examined by running various simulations with longwave radiative fluxes only.

2.5. Mixed-Layer Budget Formulation

LES results are examined using a mixed-layer budget analysis of moisture, energy, and mass, employing the moist-adiabatically conserved variables of q_T and S_l predicted by SAM. A mixed-layer budget framework provides a unique avenue for exploring the role of different mechanisms governing the evolution of the cloud field through cloud-base and cloud-thickness tendencies. We first develop mixed-layer budgets of q_T and S_l by employing a method similar to Caldwell et al. (2005), who partitioned energy and moisture into individual forcing terms, including surface fluxes, entrainment fluxes, radiative flux divergence, precipitation rates at the surface, net latent heating terms, and horizontal advection. The MLM framework is then extended using approaches similar to Wood (2007) and Ghonima et al. (2016) to yield a budget equation for cloud-base tendency in order to determine the relative importance of each budget term on regulating cloud-base/thickness tendency. Cloud-base tendency was the preferred analysis method in this particular case because of large variations of inversion-base height. In many of these runs, the LWP tendency is dominated by the inversion height tendency, since the LWP scales as the square of the cloud thickness. We instead are interested in changes to the boundary-layer saturation conditions (profiles of mixing ratio and saturation mixing ratio) from mechanisms governing the evolution of q_T and S_l budgets (e.g., entrainment or radiation) that are discernable from changes in inversion height.

The moisture budget equation determines the time-tendency of q_T, which is the sum of the water vapor q_v and liquid water mixing ratios q_l, as a function of the individual forcing terms

that act as controls on boundary-layer moisture (1). Dry air entrainment of free tropospheric air is one possible sink of boundary-layer moisture. The rate at which air is entrained into the boundary-layer is represented by the entrainment rate, w_e, and Δq_T, which represents the cloud-top jump (moisture gradient) between the cloud-layer and the free troposphere. The cloud-top jump is assumed to be a zero-order discontinuity in standard mixed-layer theory (Nicholls 1984). The product of the two aforementioned variables results in a term ($w_e \Delta q_T$) that characterizes the rate at which the boundary-layer is drying due to the incorporation of free tropospheric air into the boundary-layer. While the entrainment term represents a sink of boundary-layer moisture originating from the upper-boundary, the surface moisture flux term ($\frac{q_{Tsfcflux}}{\rho * L_v}$, also called the latent heat flux, where ρ represents the mean boundary-layer air density and L_v is the latent heat of vaporization) accounts for changes attributable to the surface boundary condition. As mentioned previously, surface fluxes are prescribed in the model and remain constant for the duration of the simulation. Another possible sink in the moisture budget is the removal of liquid water through precipitation, given by the surface precipitation rate P_0, although in our simulations this only occurs under the most extreme forcing scenarios. All the previously mentioned terms are divided by the boundary-layer depth h, which instantaneously distributes moisture changes throughout the boundary-layer. The final moisture source/sink is the mean horizontal moisture advection (tendency) term through the depth of the boundary-layer ($-\overline{\boldsymbol{v} \cdot \nabla_h q_T}$).

$$\frac{\partial q_T}{\partial t} = \frac{w_e \Delta q_T + \frac{q_{Tsfcflux}}{\rho L_v} - P_0}{h} - \overline{\boldsymbol{v} \cdot \nabla_h q_T} \qquad (1)$$

The energy budget equation determines the time-tendency of the liquid water static energy $S_l = c_p T + gz - L_v q_l$ (2), where T is temperature and g is acceleration due to gravity. The heat capacity of dry air at constant pressure c_p and L_v are considered constants, with values of 1004 J kg^{-1} K^{-1} and 2.5 × 10^6 J kg^{-1}, respectively. The energy budget is similar to the moisture budget but includes several additional terms and has units of m^2 s^{-3}. The time tendency of S_l is determined by five forcing terms shown in Equation 2. The rate at which dry, warm free tropospheric air is entrained into the boundary layer is represented by $w_e \Delta S_l$, where again, ΔS_l is the gradient between the cloudy-air and higher energy air in the free troposphere. Surface energy sources are accounted for through the sensible heat flux and is given by ($\frac{S_{lsfcflux}}{\rho}$). The energy is also altered through radiative heating/cooling, and the net radiative flux divergence is depicted by $(-R_h + R_0)$, where R_h is the net radiative flux at cloud-top and R_0 is the net radiative flux at the surface. The net radiative flux divergence was quantified simply by determining the difference in net radiative fluxes from 2-D radiation streams at the nearest index of inversion-base height and the first model grid level. Additionally, energy can be added through net latent heating, which is directly proportional to the surface precipitation rate and is denoted by $L_v P_0$. Again, the first four terms are divided by the depth of the boundary layer h. The final term in the energy budget is the mean horizontal advection (tendency) of S_l in the boundary layer $(-\overline{\boldsymbol{v} \cdot \nabla_h S_l})$.

$$\frac{\partial S_l}{\partial t} = \frac{w_e \Delta S_l + \frac{S_{lsfcflux}}{\rho} - \frac{R_h}{\rho} + \frac{R_0}{\rho} + L_v P_0}{h} - \overline{\boldsymbol{v} \cdot \nabla_h S_l} \qquad (2)$$

The mass budget can be utilized in our framework as the entrainment closure. Entrainment rate (w_e) is obtained as a residual of a cloud-top evolution equation (3) that is dependent upon the imposed large-scale vertical velocity at cloud-top ($w_s(z_i)$), advection of cloud-top heights ($-\boldsymbol{v} \cdot \nabla z_{\boldsymbol{i}}$), and the time-tendency of the inversion height ($\frac{\partial z_i}{\partial t}$) (Caldwell and Bretherton 2009). Inversion height was calculated by finding a derivative of the liquid potential temperature profile (θ_l) that was close to zero and linearly interpolated to a threshold value (0.05). Three-dimensional output was used to determine boundary layer depth column by column, with cloudy and non-cloudy columns considered and horizontally averaged across the domain. Since inversion base heights were evaluated from LES output and the advection of cloud-top heights was neglected in our Lagrangian framework, entrainment rate is a relatively straightforward calculation given our mass budget equation.

$$\frac{\partial z_i}{\partial t} + \boldsymbol{v} \cdot \nabla z_{\boldsymbol{i}} = w_e + w_s(z_i) \tag{3}$$

Although trivial theoretically, the computational accuracy of z_i is dependent upon the ability to correctly and consistently identify the inversion base in the model output and the vertical grid spacing from which the inversion base is estimated (5 m in this case). While inversion-base heights were calculated using θ_l profiles, q_T profiles were used to compute inversion-top heights due to a more distinct boundary between the inversion layer and the free troposphere. The difference between these two aforementioned heights was computed using 3-D LES output and then averaged across the model domain to estimate cloud-top jumps in S_l and q_T. The flux-jump relation discussed previously as the product of the entrainment rate and the cloud-top gradient assumes a zero-order discontinuity, however, this is a substantial source of

uncertainty in our mixed-layer budgets due to finite inversion layer thicknesses on the order of ~30 m.

Utilizing resolved entrainment fluxes from the LES provides an alternative way to directly estimate the cloud-top entrainment flux without assuming a zero-order discontinuity. Several methods of estimating entrainment fluxes from the explicit representation of S_l and q_T flux profiles were attempted to best represent the actual entrainment flux at the top of the boundary-layer. To determine how well entrainment fluxes were being represented and the overall performance of our MLM, the MLM budgets of S_l and q_T were compared to the LES budgets of S_l and q_T, with discrepancies being attributed primarily to the entrainment terms due to higher confidence in the remaining terms. Mean boundary-layer quantities of S_l and q_T in the LES were weighted by density and vertical grid spacing. Using the first-order jump model established by vanZanten et al. (1999) for convective boundary-layers (or very diffuse inversion layers), the entrainment flux was first calculated from the S_l flux profile. The S_l flux profile contains a pronounced minimum near cloud-top associated with warm, dry air entrainment. The entrainment flux is computed as the integral from the S_l flux minimum to where the S_l flux approaches zero at a higher altitude (vanZanten et al. 1999). The height indices representing the entrainment layer were used to solve for the q_T entrainment flux in the same manner. Additional methods of entrainment flux estimation include the minimum S_l flux in the cloud, a layer average from the inversion base to the S_l flux minimum (Preferred method and bottom left panel on Fig. 5), a layer average from the S_l flux minimum to the top of the cloud, and determining height indices from maximum q_T and S_l variances. Figure 5 illustrates the different entrainment flux estimation methods and the performance and limitations of the various methods are discussed in Chapter 3.

An equation for cloud-base tendency can now be derived by applying the chain rule on q_T and S_l and was expressed in Wood (2007) as (4), where z_{cb} is cloud-base height. This relationship between cloud-base tendency and the moisture and energy budgets requires two additional equations relating cloud-base changes to changes in q_T and S_l. Equation 5 presents the relationship between changes in cloud-base with respect to changes in q_T, with R_d and R_v being the gas constants of dry and moist air and T_{cb} being the temperature of the cloud-base. q_T in (5) represents the mean boundary-layer value derived from the LES profile. Heat content is assumed to stay constant and a detailed derivation of Eq. 5 can be found in Wood (2007), as well as Ghonima et al. (2015).

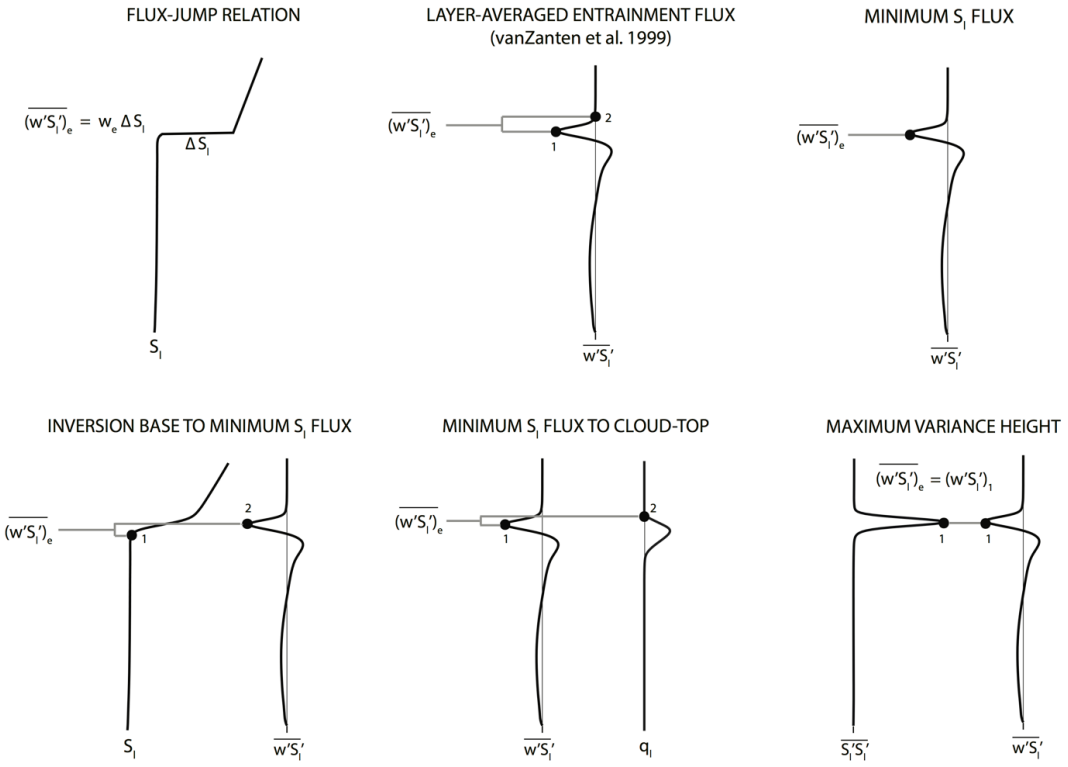

Fig. 5. Various methods for calculating entrainment fluxes. The flux-jump relation and the maximum variance height are the only two methods that treat q_T entrainment fluxes as being independent from S_l, with the other methods obtaining the height indices from S_l flux profiles to apply to the q_T flux profile. This was done due to q_T flux profiles being positive throughout the boundary-layer and no clear demarcation of downward air motion. Method used for MLM budget analysis is on the bottom left.

$$\frac{dz_{cb}}{dt} = \frac{\partial z_{cb}}{\partial q_T}\frac{\partial q_T}{\partial t} + \frac{\partial z_{cb}}{\partial S_l}\frac{\partial S_l}{\partial t} \tag{4}$$

$$\frac{\partial z_{cb}}{\partial q_T} = -\frac{R_d T_{cb}}{g q_T}\left(\frac{L_v R_d}{c_p R_v T_{cb}} - 1\right)^{-1} \tag{5}$$

$$\frac{\partial z_{cb}}{\partial S_l} = \frac{1}{g}\left(1 - \frac{c_p R_v T_{cb}}{R_d L_v}\right)^{-1} \tag{6}$$

The cloud-base response to changes in S_l is assumed to occur at constant moisture content and the relation is given by Equation 6, which was developed by Ghonima et al. (2015) to correct the original Wood (2007) formulation. The original Wood (2007) formulation failed to represent the addition/removal of heat with the use of the dry adiabatic lapse rate and only accounted for the cloud-base being a function of temperature, neglecting its dependence on pressure (Ghonima et al. 2015). The amendments made in Ghonima et al. (2015) were found to improve the Wood (2007) response to changes in heat content by approximately 22%. Both (5) and (6) are relatively constant over short time scales and in the absence of significant moisture or temperature advection.

By substituting (2), (3), (5), and (6) into (4), the final cloud-base tendency equation is produced (7). Once cloud-base tendencies are calculated, the individual contribution of each budget term on cloud-base height is analyzed and discussed. Casting in terms of cloud-thickness is done by incorporating the inversion height tendency, which must be done to appropriately ascertain the cloud evolution in the presence of a non-stationary inversion. Net cloud-base tendencies are then compared to LES cloud-base tendencies that were computed from 3-D output

using a liquid water check and interpolating to a value of 0.01 g kg^{-1}. All budget analyses were done over the 2-4 and 4-6 hour periods to avoid spin-up contamination.

$$\frac{dz_{cb}}{dt} = -\frac{R_d T_{cb}}{g q_T}\left(\frac{L_v R_d}{c_p R_v T_{cb}} - 1\right)^{-1}\left(\frac{w_e \Delta q_T + \frac{q_{Tsfcflux}}{\rho L_v} - P_0}{h} - \overline{\boldsymbol{v}\cdot\nabla_h q_T}\right) + \frac{1}{g}\left(1 - \frac{c_p R_v T_{cb}}{R_d L_v}\right)^{-1}\left(\frac{w_e \Delta S_l + \frac{S_{lsfcflux}}{\rho} - \frac{R_h}{\rho} + \frac{R_0}{\rho} + L_v P_0}{h} - \overline{\boldsymbol{v}\cdot\nabla_h S_l}\right) \quad (7)$$

CHAPTER 3

Results

3.1. Control Simulation Overview and Initial Condition Sensitivity

We found the optimal spin-up procedure to include a large-scale negative temperature tendency of 0.75 K hr^{-1} for the first 45 minutes of the simulation. We refer to this as the Control simulation. In-cloud vertical velocity variance and liquid water content were increased in comparison to the baseline simulation without the negative temperature tendency and reasonably aligned with aircraft observations (Fig. 6). The disparity in the near-surface vertical velocity variance is likely due to the aircraft encountering slightly warmer SSTs as it progressed westward. Modelled downwelling shortwave irradiance both in the cloud and near the surface were consistent with flight observations shortly after the spin-up period, while upwelling longwave fluxes in the cloud were slightly underestimated by the model (Fig. 7). The upwelling shortwave radiative flux in the cloud also matched observations well. Modelled downwelling shortwave irradiance near the surface around 2300 UTC underestimated observed fluxes, but this is likely due to the aircraft sampling clear air and highlights the difficulties of using non-Lagrangian observations to validate a Lagrangian-based LES.

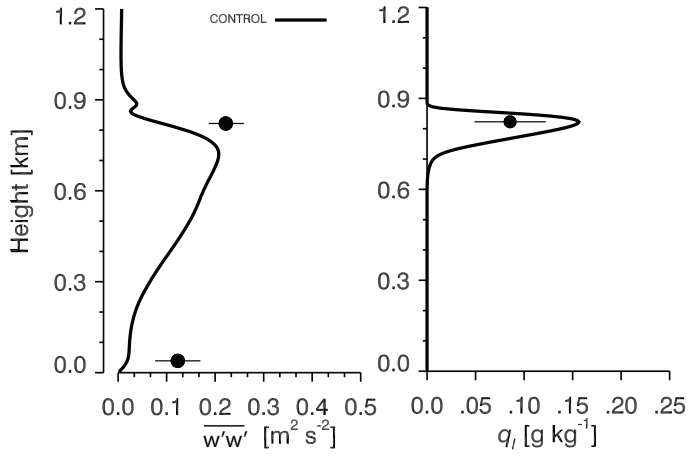

Fig. 6. Aircraft observations from level legs. Vertical velocity variance and liquid water content in the cloud retrieved from 2105-2110 UTC. Vertical velocity variance near the surface averaged from 2120-2126 UTC. Model output averaged from 2045-2145 UTC. Left panel: vertical velocity variance Right panel: liquid water mixing ratio

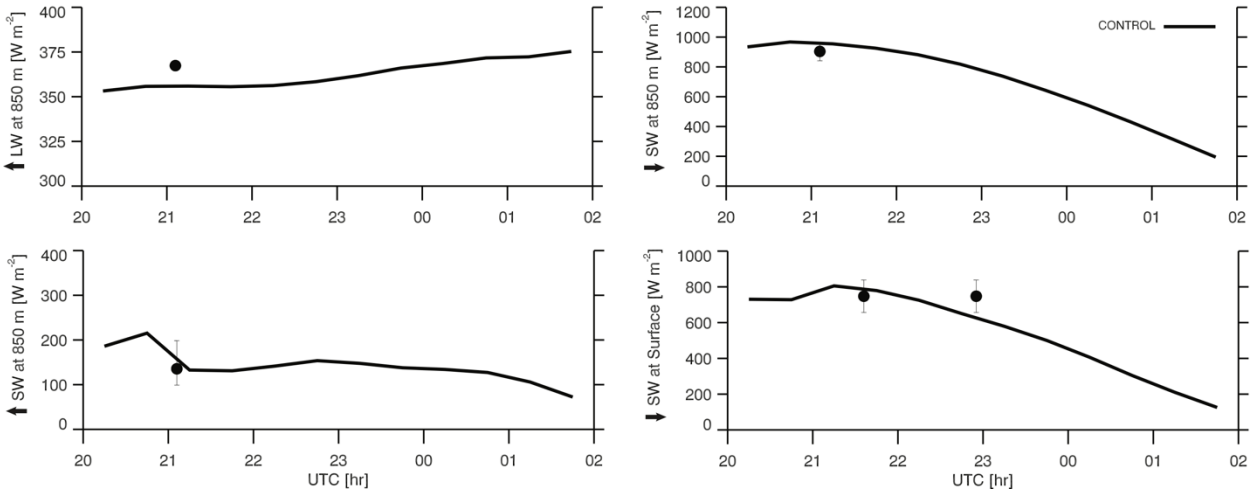

Fig. 7. Aircraft observations of radiative fluxes during level legs. Radiative fluxes averaged over duration of leg. Top left panel: Upward longwave radiative flux at 850 m Bottom left panel: Upward shortwave radiative flux at 850 m Top right panel: Downward shortwave radiative flux at 850 m Bottom right panel: Downward shortwave radiative flux at the surface.

Because the aircraft predominantly sampled conditions below 1200 m, thermodynamic profiles aloft were specified from KOAK soundings. Sensitivity to the profiles above 1200 m was tested by simulating a wide range of mid-upper level temperature profiles ($\pm$5 K from Control over the 5-21 km depth), as well as altering free-tropospheric humidity. In the warm mid-upper level temperature case the shortwave radiation budget changes are minor, but downward longwave radiation are larger, resulting in net radiation increases at the top of the boundary-layer. This increase in net radiation in the warm case leads to a slightly thinner cloud (~1-2 g m^{-2}) in terms of LWP, while the cold mid-upper level temperature case did not deviate significantly from the Control (Fig. 8). Free-tropospheric humidity sensitivity was evaluated through adjusting water vapor mixing ratios at 1500 m from 0.5-3 g kg^{-1}. Lower free-tropospheric moisture resulted in a similar LWP evolution as the Control for the 2-4-hour period, but began to dissipate at a faster rate in the 4-6-hour period. Higher free-tropospheric moisture lowered LWP by ~1-4 g m^{-2} for most of the simulation, but ended near the Control LWP. Overall, sensitivity to free-tropospheric moisture is minimal because of higher moisture content limiting the strength of dry air entrainment and the lower moisture content increasing longwave and evaporative cooling efficiency (Wood 2012).

The Control simulation exhibited a slowly diminishing LWP after spin-up, with a reduction of 7.1 g m^{-2} over the course of the simulation (Fig. 8). Cloud fraction remained near unity and never fell below 0.95 (not shown). Mean profiles of relevant boundary-layer quantities are shown in Figure 9. The post-spin-up cloud field was roughly 200 m thick and gradually thinned to 160 m, with a peak liquid water content of 0.15 g kg^{-1} that varied minimally. Mean boundary-layer TKE monotonically increased in time despite decreasing cloud-top buoyancy integrals. Entrainment flux integrals in the 2-4-hour period were larger than 4-6 hour averages,

but buoyant production of TKE was stunted by the initial stratification in the q_T profile. A small increase in vertical velocity variance was evident near cloud-top, and through a TKE budget analysis this was found to be caused by weak shear-production of TKE (Appendix A). Inversion heights fell nearly 100 m over the course of the simulation as subsidence rates exceeded entrainment. Cloud-top jump calculations indicate a gradual increase in stability of the inversion throughout the afternoon. The combination of low liquid water contents yet effective longwave cooling lead to a scenario where the cooling boundary-layer allowed the cloud to remain relatively stable throughout the afternoon through limited entrainment and weak surface moisture fluxes. A simulation with no surface fluxes established that the minimal latent heat fluxes (4.45 W m^{-2}) play a very modest role in increasing LWP and cloud lifetime, only contributing to a difference of about 1 g m^{-2}.

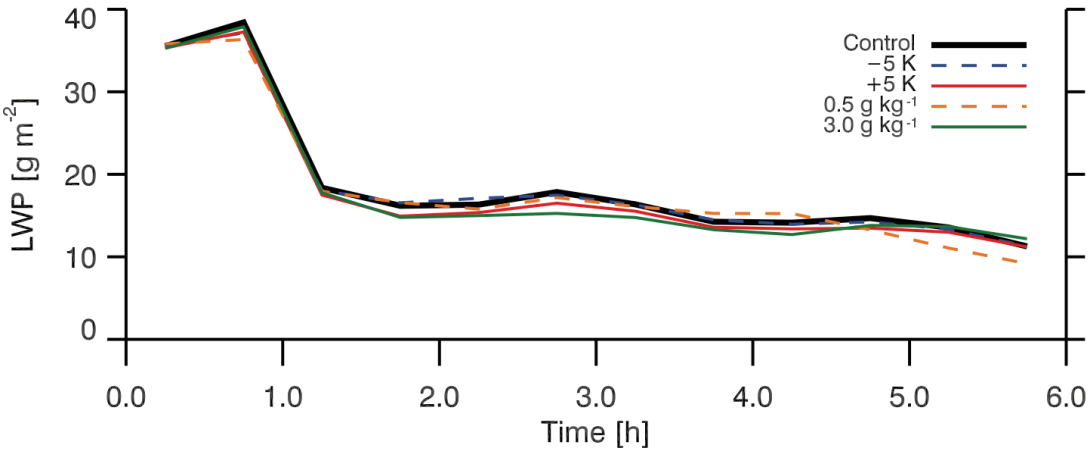

Fig. 8. Liquid water path (LWP) of initialization sensitivity runs.

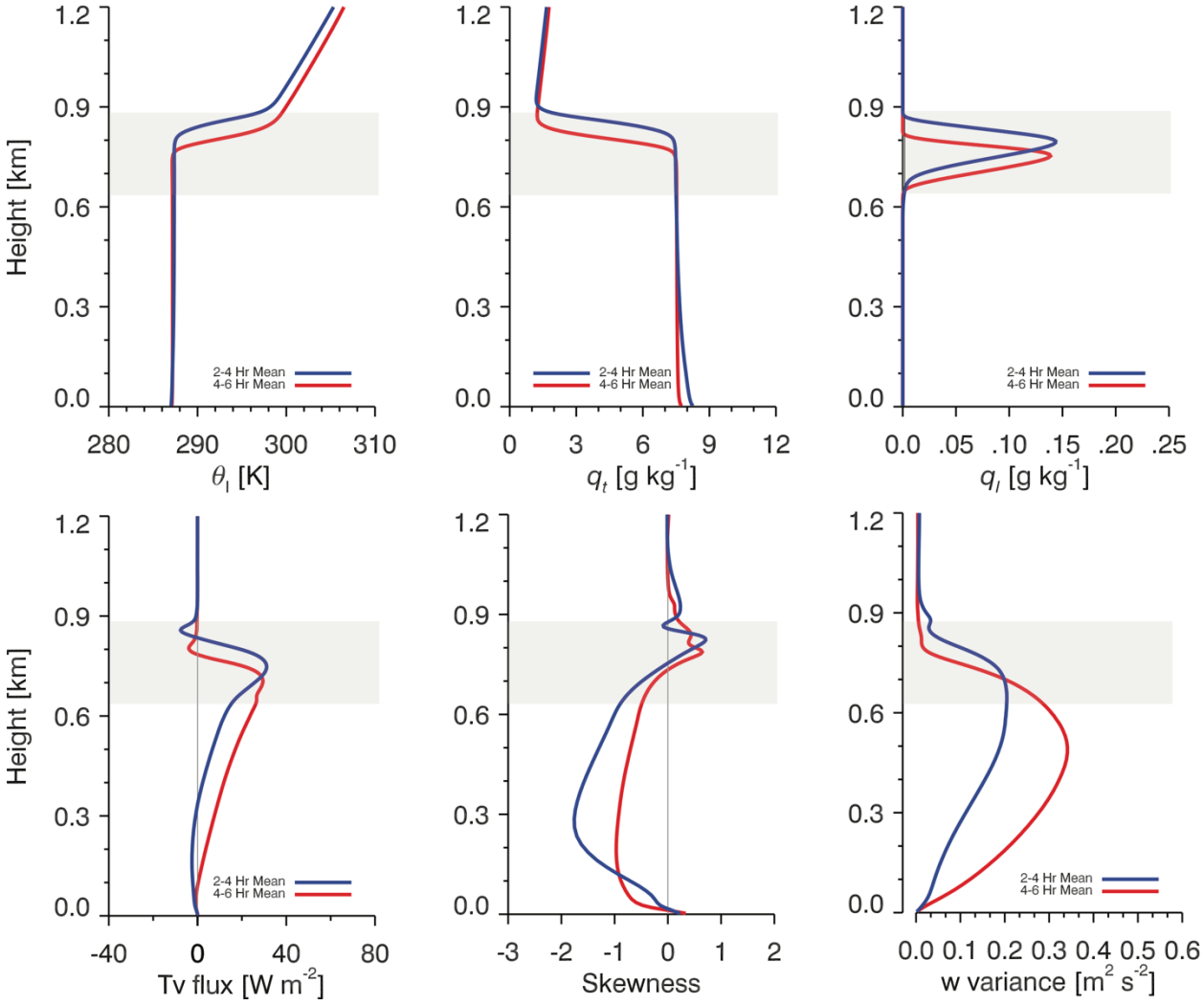

Fig. 9: Liquid potential temperature (θ_l), total water mixing ratio (q_T), liquid water mixing ratio (q_l), buoyancy flux (T_v flux), vertical velocity skewness, and vertical velocity variance 2-4 and 4-6-hour mean profiles for the Control run. Cloud region shaded in gray.

3.2. Sensitivity to Variations in Environmental Forcing

a.) Subsidence Sensitivity

The range of subsidence velocities indicated a near perfect negative linear correlation between subsidence rate and liquid water content in both the 2-4 and 4-6 hour averaging periods, with r^2 values greater than 0.95. Mean-BL TKE remains similar for cases where LWP exceeds 10 g m^{-2} for the duration of the run (Fig. 10), despite substantially different negative cloud-top buoyancy fluxes. In general, decreasing subsidence scales linearly with mean boundary-layer depth, where a 1 cm s^{-1} increase in subsidence velocity results in approximately a 100 m shallower boundary-layer over the course of the simulation. Although weaker subsidence runs result in deeper boundary-layers and thus higher cloud-tops, the increased entrainment produces higher cloud-top temperatures and slightly increased longwave cooling efficiency owing to a decrease in air density (Stephens et al. 1978), which in turn causes greater longwave radiative flux divergence. Additionally, thicker clouds and higher liquid water contents have a higher bulk infrared emissivity, approximated by the idealized functional dependence derived by Chylek and Ramaswamy (1982). Figure 11 shows increasing entrainment fluxes with weaker subsidence (-0.75 – 0 cm s^{-1}), likely stemming from the increasing longwave radiative flux divergence. The decoupling is evident with peak vertical velocity values occurring in the cloud-layer and sub-cloud negative buoyancy fluxes, with the intrusion of warm, dry air into the cloud that is not able to be effectively mixed throughout the deeper boundary-layer.

Analysis of a decoupling parameter formulated by Park et al. (2004), which is calculated as the difference of cloud and sub-cloud q_T and S_l divided by the difference of q_T and S_l just above the inversion layer ($q_{Tinvtop+1}$) and the sub-cloud layer (8; same equation for S_l), suggests that weaker subsidence produces stronger boundary-layer stratification that persists longer, in

contrast to the Control (Appendix B), which is able to mix out most of the initial stratification. The increased stratification ultimately limits the spread in mean-BL TKE trajectories. While stronger subsidence implies a stronger inversion through enhanced compressional warming, the reduced cloud water in the stronger subsidence cases plays an important role in inversion structure. Sensitivity experiments involving only longwave radiative fluxes demonstrated that efficient longwave cooling maintains the inversion strength, but in the presence of shortwave radiation the reduction in LWP seen under strong subsidence cases cannot maintain the sharp inversion structure (Fig. 12).

$$Decoupling\ Parameter = \frac{q_{Tcld} - q_{Tsubcloud}}{q_{Tinvtop+1} - q_{Tsubcloud}} \tag{8}$$

Results from our suite of subsidence rate simulations are in agreement with recent studies performed by Myers and Norris (2013) and Van der Dussen et al. (2016). Myers and Norris (2013) determined observationally that given a fixed value of inversion strength, decreasing subsidence would promote greater LWP. Since our weaker subsidence simulations were able to maintain inversion strength through stronger cloud-top cooling, the Myers and Norris (2013) assertion seems to hold true. Van der Dussen et al. (2016) found that solar absorption stunts the growth of the boundary-layer initially, but eventually grows at a faster rate as entrainment rates increase later in the afternoon. Our simulations display a similar response, with the weaker subsidence runs having entrainment rates that typically monotonically increase with time.

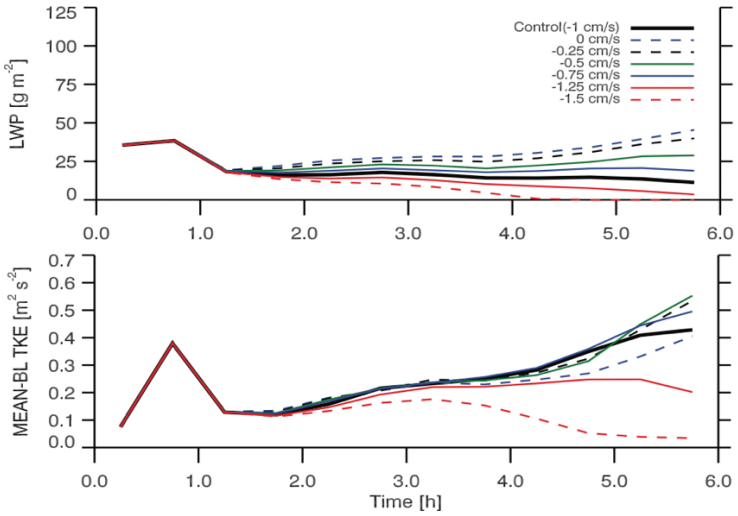

Fig. 10: Liquid water path (LWP) and mean-BL TKE for the range of subsidence values of 0-1.5 cms^{-1}

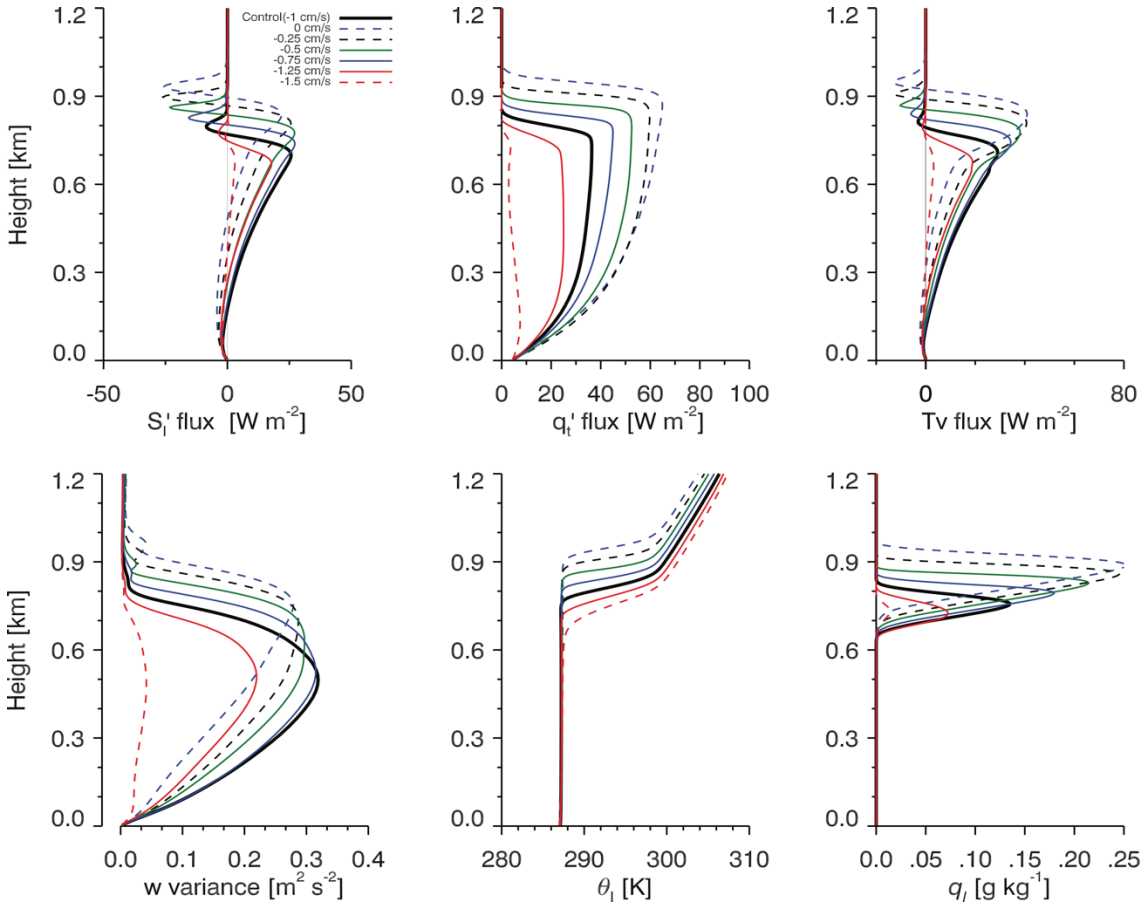

Fig. 11. 4-6 hour mean profiles of Top Row (left to right): S_l entrainment flux, q_T entrainment flux, buoyancy flux Bottom Row (left to right): vertical velocity variance, liquid potential temperature (θ_l), and liquid water mixing ratio (q_l).

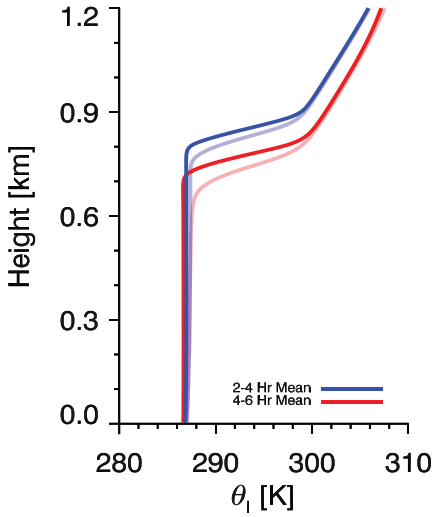

Fig. 12: Dimmed lines: SW/LW 1.5 cm/s subsidence Bold lines: LW only 1.5 cm/s subsidence

b.) Large-Scale Moisture/Temperature Tendency Sensitivity

Moisture and temperature tendencies were altered to determine the sensitivity of cloud properties to changing water vapor and saturation vapor pressures, respectively. The addition of moisture has a direct and predictable influence on LWP from first principles, as cloud-bases would be expected to fall given higher mixing ratios and θ_l values that do not change dramatically. Negative moisture tendencies ranging from 0.25-1.0 g kg^{-1} hr^{-1} resulted in desiccation and rapid cloud break-up before the 3-hr mark. As liquid water was depleted there was a concomitant decrease in mean boundary-layer TKE associated with the removal of the longwave cloud-top cooling. Even though moisture tendencies were applied homogeneously throughout the depth of the boundary-layer, moisture pooling in the lower half was evident in q_T profiles of both negative and positive moisture tendencies (Fig. 13). This uneven distribution of q_T with height can destabilize the boundary-layer and promote isolated surface-based updrafts, but stronger solar absorption and increased warm air entrainment in higher liquid water content runs warms the cloud-layer and increases stability of the boundary-layer θ_l profile. The strong

positive moisture tendency case developed fog and drizzle rates of 0.8-1 mm day^{-1} in the latter half of the simulation that encouraged further stratification. Vertical velocity variance profiles indicate the inability for positive moisture tendency runs to effectively distribute turbulent energy throughout the depth of the boundary layer, similar to the weak subsidence runs, as the higher variances remain closer to cloud-top. Peak radiative cooling rates near cloud-top increase with increasing moisture input, but only to a threshold value where the cloud becomes significantly optically thick, which reduces longwave cooling efficiency.

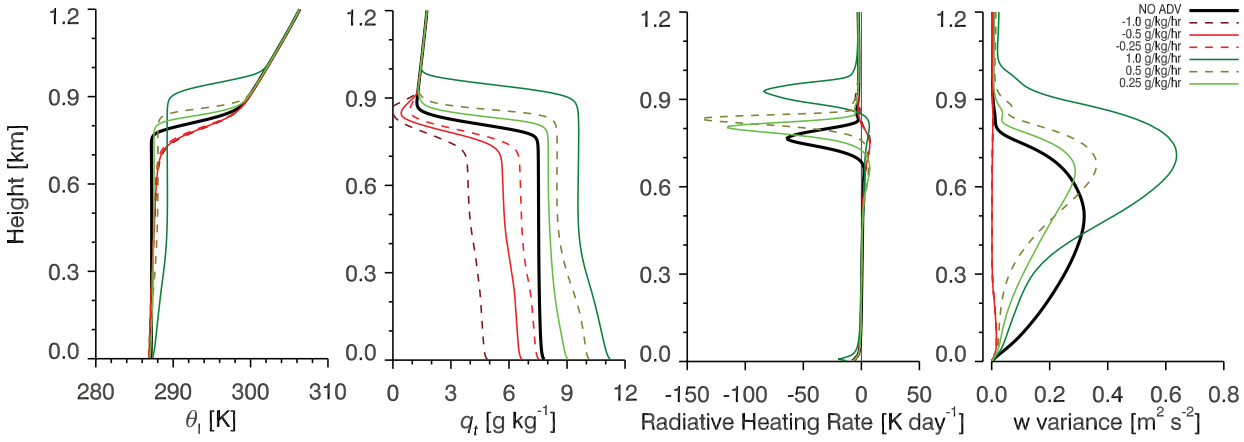

Fig. 13. 4-6 hour mean profiles of Top Row: θ_l, q_T Bottom Row: Radiative heating rate and vertical velocity variance. NOADV represents the Control run.

Negative temperature tendencies affects moisture indirectly by lowering saturation vapor pressures according to the Clausius-Claperyon relation, thus resulting in lower cloud-bases for a given moisture content. As was the case with negative moisture tendencies, any initial perturbation that thins the cloud resulted in rapid cloud dissipation. A mean boundary-layer warming of 0.5-0.75 K in the weak positive temperature tendency case resulted in dissipation that occurred only 2 hours after spin-up. The development of significant drizzle rates (3-7 mm

day^{-1}) in medium (-1.0 K hr^{-1}) and strong (-2.0 K hr^{-1}) negative temperature tendency cases limits the spread in final mean-BL TKE values (Fig. 14). Negative temperature tendencies confined to the boundary-layer inherently increases static stability of the inversion while simultaneously decreasing evaporative potential through a reduction in cloud-top moisture gradients (Fig. 15). Initially, the medium negative temperature tendency simulation did not produce sufficiently strong sub-cloud turbulence, which lead to decoupling. A positive skewness profile indicates the strong negative temperature tendency simulation results in surface-based convection. Negative cloud-top buoyancy fluxes in the 2-4-hour period increase commensurately with LWP, but as the clouds become thicker this relationship no longer exists due to changes in radiative flux divergence, which will be discussed in detail in Section 3.5b.

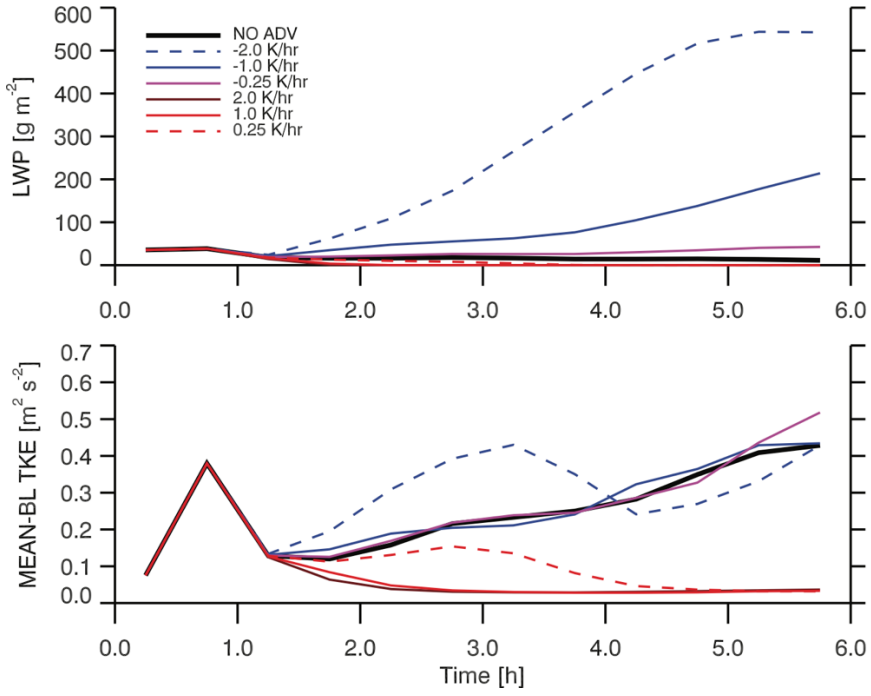

Fig. 14. Liquid water path (LWP) and mean-BL TKE for the range of temperature tendency forcing (-2.0 – 2.0 K hr^{-1})

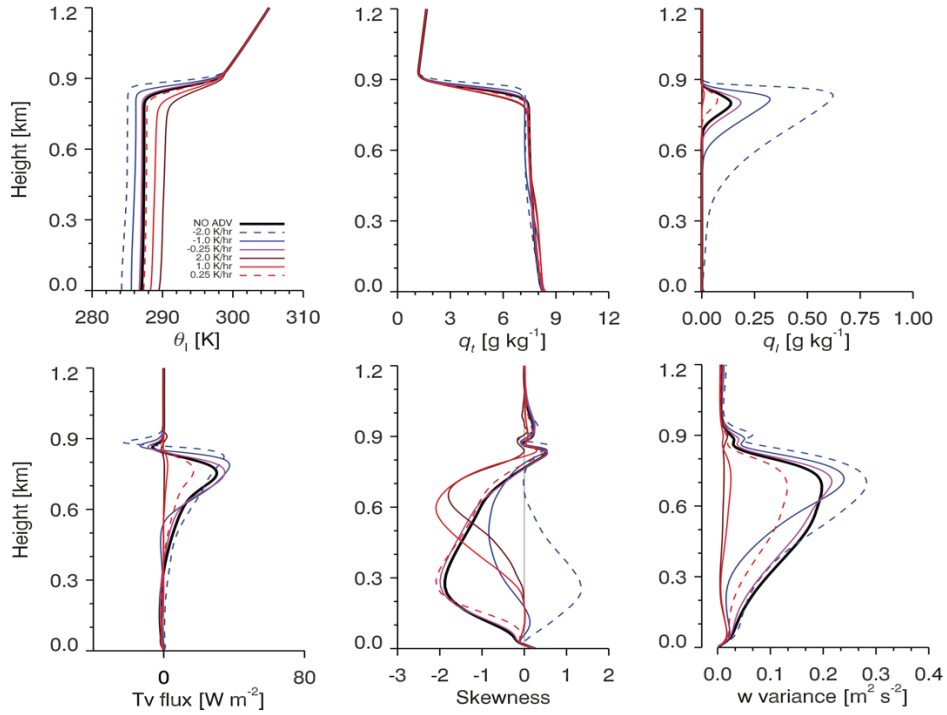

Fig. 15. 2-4 hour mean profiles of Liquid potential temperature (θ_l), total water mixing ratio (q_T), liquid water mixing ratio (q_l), buoyancy flux (T_v flux), vertical velocity skewness, and vertical velocity variance.

c.) Surface Flux Sensitivity

Altering surface boundary conditions can emulate a variety of scenarios for stratocumulus clouds, including increased sensible heat fluxes (SHF) over land and higher latent heat fluxes (LHF) associated with warmer SSTs. The surface fluxes were prescribed at a constant value for the duration of the simulations, and as a result no feedbacks that would naturally influence surface fluxes were represented. In sensitivity runs where sensible heat fluxes were large (100-150 W m^{-2}), the response was to greatly increase mean-BL TKE through surface buoyancy production. The increased surface buoyancy production leads to enhanced entrainment rates and cloud-thinning. These findings are also corroborated by Ghonima et al. (2016), using LES and MLMs to determine stratocumulus lifetime given various surface forcings. Increasing LHF has been extensively studied in SCTs and found to be a primary mechanism for decoupling

through enhancing entrainment fluxes, which disproportionately dry the cloud-layer (de Roode et al. 2016; Chung et al. 2012). However, our simulations suggest the increased entrainment fluxes were compensated by more efficient longwave cooling and a constant moisture supply from below. Boundary-layer depth does not vary considerably, with deviations from the Control being on the order of 10 m, suggesting the larger entrainment rates are still not sufficient to counteract subsidence. Regardless of substantial q_T stratification in the subcloud layer, the LHF simulations imply no apparent decoupling in vertical velocity variance structure or buoyancy fluxes (Figure 16). The strong LHF case (150 W m^{-2}) shows signs of cumulus-coupling associated with the moisture stratification, which manifests itself as positive skewness in the sub-cloud layer (de Roode and Duynkerke 1996).

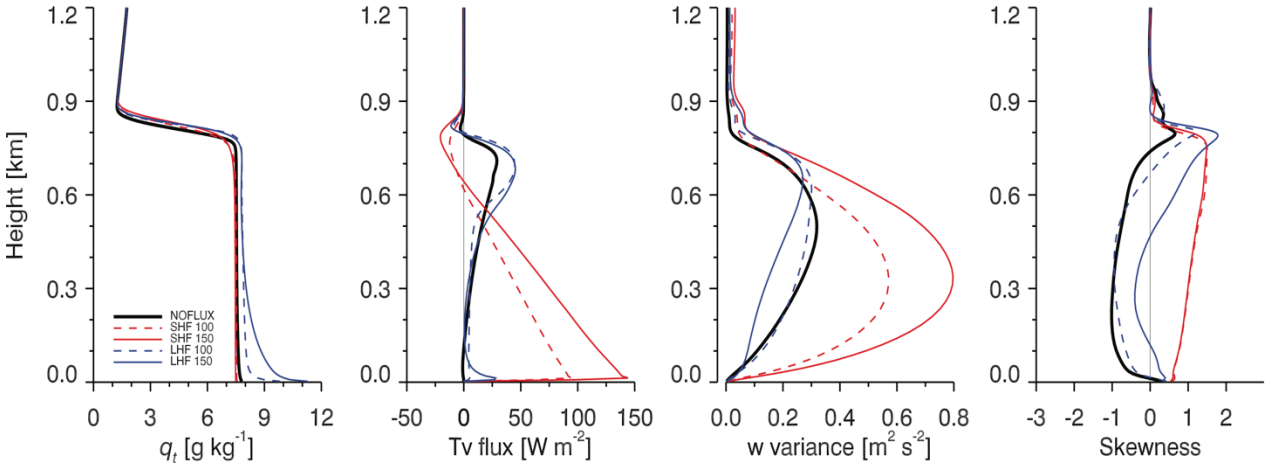

Fig. 16: 4-6-hour mean profiles of total water mixing ratio q_T, buoyancy flux (Tv flux), vertical velocity variance (w variance), and Skewness for SHF/LHF ranging from 100-150 Wm^{-2}

d.) Shear Sensitivity

Although much of the previous focus has been on the buoyancy production/consumption of TKE, wind shear near the inversion often has an important influence on cloud-top mixing and inversion structure, especially in our study region off the California coast where a coastal jet is frequently observed (Wang et al. 2008). Overall, our LES results corroborate previous findings on the effects of wind shear on turbulent production and cloud evolution. Increased wind shear resulted in lower liquid water content and reduced mean-BL TKE through the enhancement of cloud-top mixing. As the cloud-water is diminished the production of negative cloud-top buoyancy is limited and entrainment rates are reduced. Inversion heights were found to decrease as wind shear was increased, which Wang et al. (2008) determined would occur under weaker and more diffuse inversions. Initially, cloud-top mixing is increased through enhanced shear-production of TKE, but an attendant decrease in entrainment rate occurs as liquid water content is reduced considerably. Figure 17 shows the evolution of inversion depth and inversion base height, as well as the existence of a deep cloud-free turbulent sublayer within the inversion, which has been observed and modeled in previous studies exploring the gap between cloud-top and turbulent mixing interfaces (Lenschow et al. 2000; Moeng et al. 2005). Speed shear simulations associated with equal magnitudes of positive and negative horizontal vorticity are not equivalent, with positive speed shear producing greater TKE through the relaxation of the winds above 1500 m. This is likely because the stronger free-tropospheric wind magnitude in the positive horizontal vorticity simulation is likely better able to sustain the shear (and hence the shear-production of TKE) at the top of the boundary-layer.

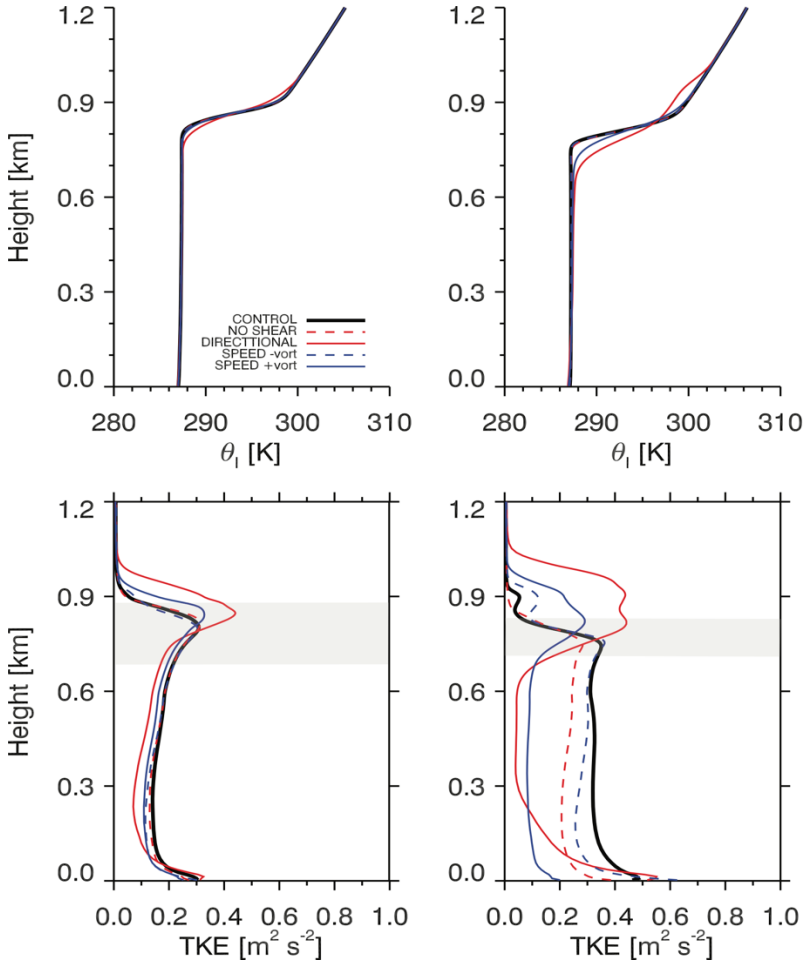

Fig. 17: Left Column: 2-4-hour mean profile of θ_l (Top) and TKE (Bottom) Right Column: 4-6-hour mean profile of θ_l (Top) and TKE (Bottom). Gray shaded region represents mean cloud-layer of the directional shear run (DIRECTIONAL).

e.) Radiative Forcing Sensitivity

Radiative forcing sensitivity was investigated by examining LES output under various forcing scenarios in the absence of shortwave radiation, in an attempt to isolate the implications of shortwave absorption. Nocturnal stratocumulus have been extensively studied observationally and through various modeling approaches, given the near-equilibrium/steady-state behavior. Stronger convective circulations are observed at night as longwave cooling drives negative buoyancy production and the boundary-layer remains well-mixed. This efficient coupling with

the surface moisture supply for cases of larger surface evaporation/LHF is crucial for sustaining the cloud (Turton and Nicholls 1987), but in our Control case, moisture flux from the ocean surface is so small that the increased entrainment is not compensated by a more efficient water vapor flux from the surface and LWP decreases slightly with time. Cases with stronger surface moisture flux could possibly maintain the cloud LWP against drying from entrainment.

3.3. Mixed-Layer Budget Uncertainties

The mixed-layer assumption naturally assumes the boundary-layer to remain well-mixed, and departures from the well-mixed state are manifested as errors in the mixed-layer model diagnosis. In the LES, stratification is often manifested by negative buoyancy fluxes near cloud-base, or a significant minimum in cloud-base vertical velocity variance (Bretherton and Wyant 1997; Stevens et al. 2005). Afternoon stratocumulus clouds are particularly susceptible to decoupling from solar absorption (Albrecht et al. 1988) and the uneven distribution of buoyancy flux throughout the boundary layer, primarily due to large in-cloud liquid water fluxes (Bretherton and Wyant 1997). Despite afternoon conditions that oftentimes support decoupling, small latent and sensible heat fluxes over the cool ocean surface limited the stratification in the Control run, and the boundary layer was able to remain relatively well-mixed.

The calculation of entrainment fluxes presents an additional source of uncertainty, because our case clearly deviates from standard mixed-layer theory, with a diffuse inversion and cloud-tops that do not directly coincide with the inversion base. Traditionally, the entrainment interface is thought to be a sharp transition layer that separates turbulent, saturated air from laminar, unsaturated free-tropospheric air (Randall 1980). However, Moeng et al. (2005) found that the cloud-top interface and the depth of the boundary-layer mixing are separated by a fairly

significant depth (~10-20 m). In order to best represent the nature of the air near the entrainment interface, several ad hoc methods of entrainment flux estimation were attempted, summarized in Fig. 5, and the performance of the MLM was gauged by a comparison of LES S_l and q_T budgets. The absolute relative error was calculated according to (9), with x_{obs} being the LES budget tendency and x_{mlm} being the MLM budget tendency. The flux-jump relation (e.g., $w_e \Delta q_T$) is inapplicable in this first-order inversion jump case and vastly overestimates entrainment warming and drying, whereas the layer-averaged entrainment fluxes (vanZanteen et al. 1999) grossly underestimates the entrainment warming and drying. Averaging the entrainment fluxes from the minimum S_l flux to the cloud-top significantly underestimated entrainment drying while only slightly underestimating warming. Using the height of the maximum variance performed reasonably well for the S_l budget, but underestimated entrainment drying. The height of the minimum S_l flux produced similar results to our chosen method in the 2-4-hour period, but overestimated entrainment warming in the 4-6-hour period. The layer-average of the flux from the inversion base to the minimum S_l flux was the most robust method in terms of reconciling with LES budgets.

$$Abs.Rel.Err. = \left| \frac{x_{mlm} - x_{obs}}{x_{obs}} \right| \tag{9}$$

In general, 2-4-hour mean q_T MLM tendencies indicate too much drying in the MLM with 70% of the available simulations (24 simulations had cloud water present during the 2-4-hour period) overestimating drying (Appendix C). Only the two latent heat flux sensitivity simulations (with latent heat flux values of 100 and 150 W m^{-2}) underestimate drying, with absolute relative errors greater than 0.2 in the first analysis period. The 4-6-hour mean q_T MLM tendencies suggest underestimation of drying, with 76% of the simulations (20 simulations had

cloud water present during the 4-6-hour period) exhibiting boundary-layers that are too moist. There is no clear bias in 2-4-hour mean S_l MLM tendencies, however, major absolute relative errors in excess of 1 occur 6 times during the 2-4-hour period (25% of simulations), while only occurring once in the 4-6-hour period. 4-6-hour mean S_l MLM tendencies underestimate warming 80% of the time, with only 3 simulations overestimating warming. Overall, absolute relative errors greater than 0.2 in the MLM budgets are ~45% more likely in the 2-4-hour period than in the 4-6-hour period. The error analysis suggests our method consistently underestimates the total change in the depth of the entrainment layer, with layers that are generally too shallow in the 2-4-hour period and too deep in the 4-6-hour period. We speculate that these errors emerge from increasing static stability with time and a fundamentally different turbulent structure near cloud-top during the two analysis periods that our current method of entrainment flux calculation is not able to fully capture (Appendix D). Also, there are 11 instances of overestimating one budget while underestimating the other, which may suggest that the entrainment flux layer associated with S_l and q_T are not necessarily collocated. Regardless of the aforementioned uncertainties, meaningful deductions can be made from the analysis of individual budget terms.

3.4. Control Mixed-Layer Budget Analysis

Figure 18 and Table 1 show the individual budget terms contributing to changes in the MLM cloud-base tendency equation (7), along with the net cloud-base tendency diagnosed by the MLM (the sum of the terms on the right-hand side of (7), denoted as "Net" in Fig. 18) and the cloud-base tendency derived from LES results. Changes in cloud-base height are governed by the entrainment warming/drying and shortwave absorption, which act to raise the cloud base, and longwave cooling, which acts to lower the saturation point and thicken the cloud. The stronger

stratification in the first analysis period leads to fairly large discrepancies between the MLM and the LES. The budget and stratification errors can be isolated by inputting model budget tendencies into (7). Budget errors are responsible for an overestimation of entrainment drying of approximately 0.13 cm s^{-1} and an underestimation of drying of about -0.05 cm s^{-1} in the 2-4 and 4-6-hour periods, respectively. The remainder of the errors are attributed to decoupling and the accuracy of the model-derived cloud-base, which is limited by vertical grid spacing. As the boundary-layer becomes well-mixed the MLM cloud-base tendencies are more aligned with the LES. Even in the presence of substantial shortwave heating the entrainment fluxes are not shut down in this case. Entrainment fluxes in both analysis periods are likely comparable in size, but definitive conclusions about the evolution of the magnitude of the entrainment fluxes cannot be

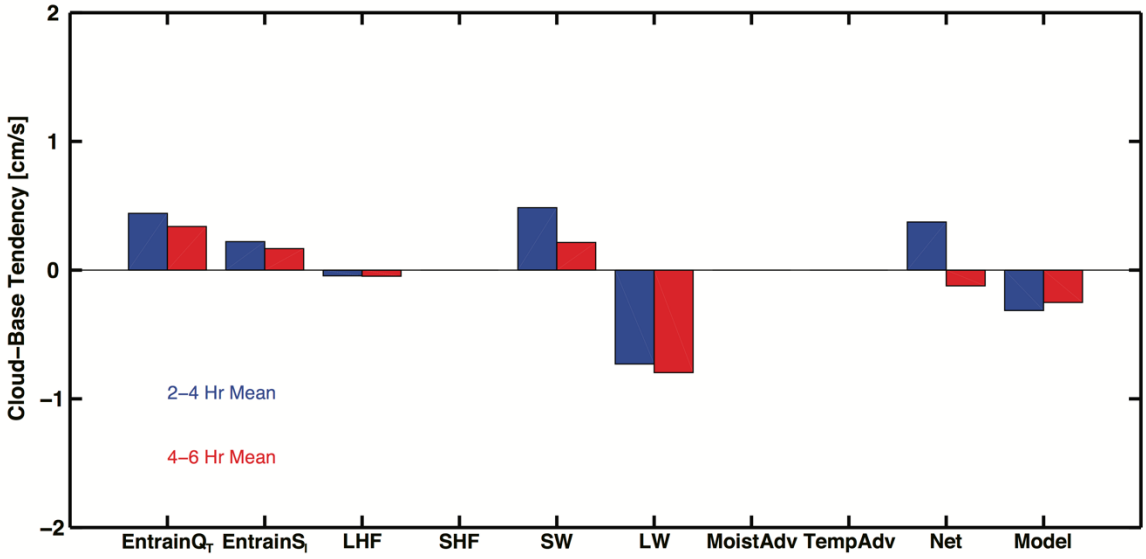

Fig. 18. Individual budget terms from left to right: q_T entrainment flux (EntrainQ$_T$), S_l entrainment flux (EntrainS$_l$), latent heat flux (LHF), sensible heat flux (SHF), shortwave radiative flux divergence (SW), longwave radiative flux divergence (LW), moisture advection (MoistAdv), temperature advection (TempAdv), Net of budget terms, LES cloud-base tendency (Model). Negative values indicate a lowering of the cloud-base.

drawn in this particular case because of uncertainties regarding boundary-layer stratification. However, the budget terms indicate that the effect on cloud-base decreases in boundary-layer moisture caused by the entrainment of dry air is likely larger than the changes to the saturation point associated with the entrainment of warmer (higher liquid water static energy) free tropospheric air. The small amount of surface moisture flux (LHF) plays a minor role in reducing cloud-base heights, and remains nearly constant in time as temperature of the cloud-base and the depth of the boundary-layer do not drastically change the small fixed value. Shortwave warming contributes to cloud-base rises and decreases substantially from the first to second analysis period, as expected with decreasing insolation as the afternoon progresses. The main source of boundary-layer cooling is through longwave flux divergence, which remains fairly constant in time, increasing slightly in the 4-6-hour period because of the shallower boundary-layer. In this thin cloud case, the longwave cooling was able to overcome the drying and warming terms to result in a net cooling and lowering of the cloud-base. Figure 19 shows the cloud-thickness tendency throughout the afternoon, with cloud-thickness decreasing despite falling cloud-bases, as the inversion base is decreasing faster than the cloud-base is lowering.

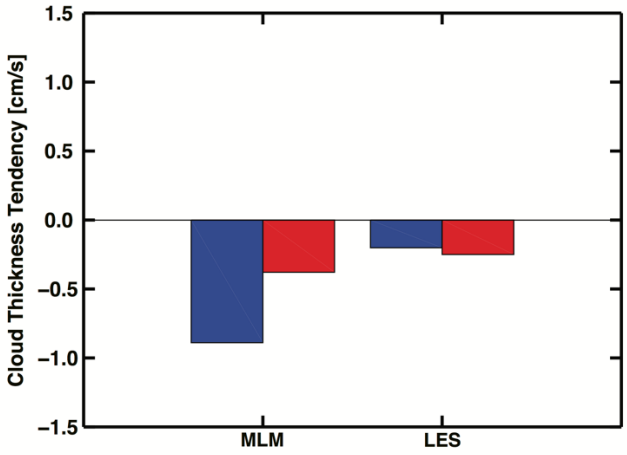

Fig. 19. Cloud thickness tendency accounting for tendency inversion height tendency. MLM cloud thickness on left. LES cloud thickness on the right. Negative values indicate a thinning cloud.

3.5. Sensitivity Tests Mixed-Layer Budget Analysis

a.) Subsidence Simulations Budget Analysis

As subsidence weakens from -1.5 to 0 cm s^{-1}, the cloud-base rises associated with the q_T and S_l entrainment fluxes increase, with the q_T entrainment flux once again contributing to greater cloud-base rises than S_l entrainment fluxes (Table 1). Relative to the control run the shortwave radiative flux divergence contribution to cloud-base tendency did not vary over 0.03 cm s^{-1} in all cases, indicating an insensitivity stemming from the increase in boundary-layer depth. The longwave radiative flux divergence relative importance also remains steady, increasing with weakening subsidence by no more than 0.10 cm s^{-1}. While net radiative flux divergence remains nearly constant between varying subsidence cases, the weaker subsidence runs are not able to counteract the enhanced entrainment fluxes, resulting in boundary-layer warming and drying and a rise in cloud-base. As the afternoon progresses, the reduction in shortwave flux divergence is enough to overcome the enhanced entrainment and cloud-base falls

ensue. Table 1 compares the individual budget terms of the control and the 0.25 cm s^{-1} subsidence run. The MLM S_l budget tendency in the 2-4-hour period underestimates the warming (Appendix C), which is more than likely attributable to an underestimation of the S_l entrainment fluxes. As discussed in Section 3.2a, under weaker subsidence the boundary-layer was not able to reach a well-mixed state by the end of the second period and remained slightly decoupled, which we speculate is responsible for most of the deviations from the LES ("Model" term).

Table 1. Comparison of the Control and 0.25 cm s^{-1} cloud-base tendency budget terms (cm s^{-1})

CONTROL	**EntrainQ$_T$**	**EntrainS$_l$**	**LHF**	**SW**	**LW**	**Net**	**Model**
2-4 Hr	0.44	0.22	-0.044	0.48	-0.73	0.37	-0.31
4-6 Hr	0.34	0.17	-0.047	0.21	-0.80	-0.12	-0.25
0.25 cm s^{-1}	**EntrainQ$_T$**	**EntrainS$_l$**	**LHF**	**SW**	**LW**	**Net**	**Model**
2-4 Hr	0.54	0.33	-0.042	0.51	-0.79	0.55	0.09
4-6 Hr	0.51	0.31	-0.042	0.22	-0.85	0.14	-0.23

b.) Moisture/Temperature Tendency Budget Analysis

MLM q_T tendencies agree well with model q_T tendencies in positive moisture tendency simulations with relative errors remaining below 0.15 (Appendix C). Slightly larger relative errors (0.07-0.31) are present in the S_l budget, with all of the positive moisture tendency simulations underestimating the higher energy budget tendencies. Errors related to the budgets are no larger than 0.50 cm s^{-1}, while errors associated with decoupling are larger than the

Control. Figure 20 shows the individual budget terms for the weak positive moisture tendency simulation (0.25 g kg^{-1} hr^{-1}). The LES cloud-base tendency appears to suggest a slower lowering than the MLM in the early period, even though the stratification should result in overestimation of cloud-base height in the MLM, and we expect this to be associated with errors in the average cloud-base height calculation in the LES. Entrainment fluxes of q_T and S_l increase from the 2-4 to 4-6-hour period in all positive moisture tendency cases (Appendix E). Again, q_T entrainment flux contributes to a greater change in saturation than the S_l entrainment flux. In spite of the larger 4-6-hour entrainment fluxes, the reduction of shortwave warming is enough to compensate for this change and produces slower positive S_l tendencies and cloud-thickness tendency increases with time.

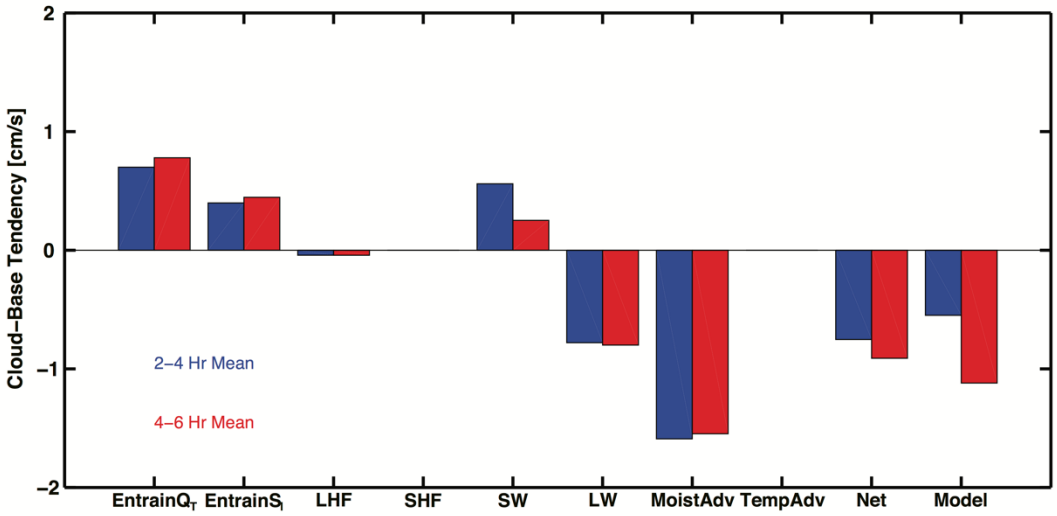

Fig. 20. Same as Fig. 18, but for a positive moisture tendency of 0.25 g kg^{-1} hr^{-1}

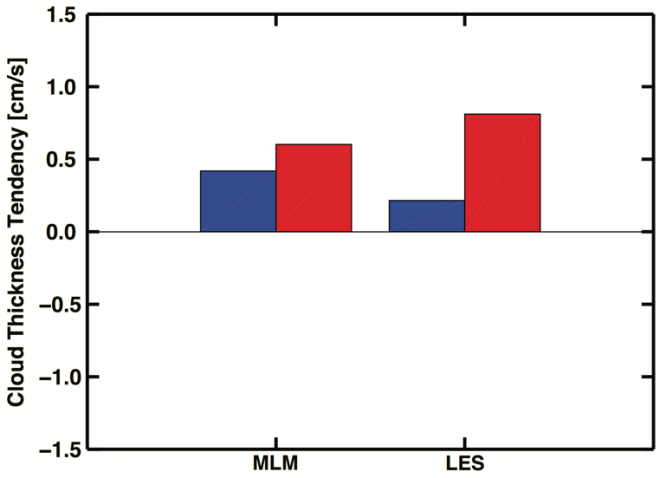

Fig. 21. Same as Fig. 19, but for a positive moisture tendency of 0.25 g kg^{-1} hr^{-1}

Contrary to the positive moisture tendency runs, negative temperature tendencies cool and dry instead of moisten and warm the boundary-layer. Decoupling measures indicate similar values of stratification between the Control and weak negative temperature tendency runs (Appendix B), but the medium and strong negative temperature tendency simulations (-1 and -2 K hr^{-1}) remain decoupled for the duration of the run. Figure 22 shows the cloud-base tendency budget terms for the medium negative temperature tendency run. The longwave flux divergence decreases with a cooling boundary-layer, as a result of lower cloud-top temperatures. The decrease in longwave cooling and the decrease in warming from solar absorption result in a minimal net cooling effect in the 4-6-hour period. This results in cloud-bases that fall faster early in the afternoon, when entrainment fluxes are smaller. Light drizzle occurs in the medium negative temperature tendency case, but the effects of diabatic heating and moisture loss from surface precipitation are negligible ($< 7 \times 10^{-6}$ cm s^{-1}). The positive values of cloud-thickness

tendency modestly decrease in time associated with the slight increase in entrainment in the 4-6-hour period arising from isolated cumulus updrafts (Fig. 23).

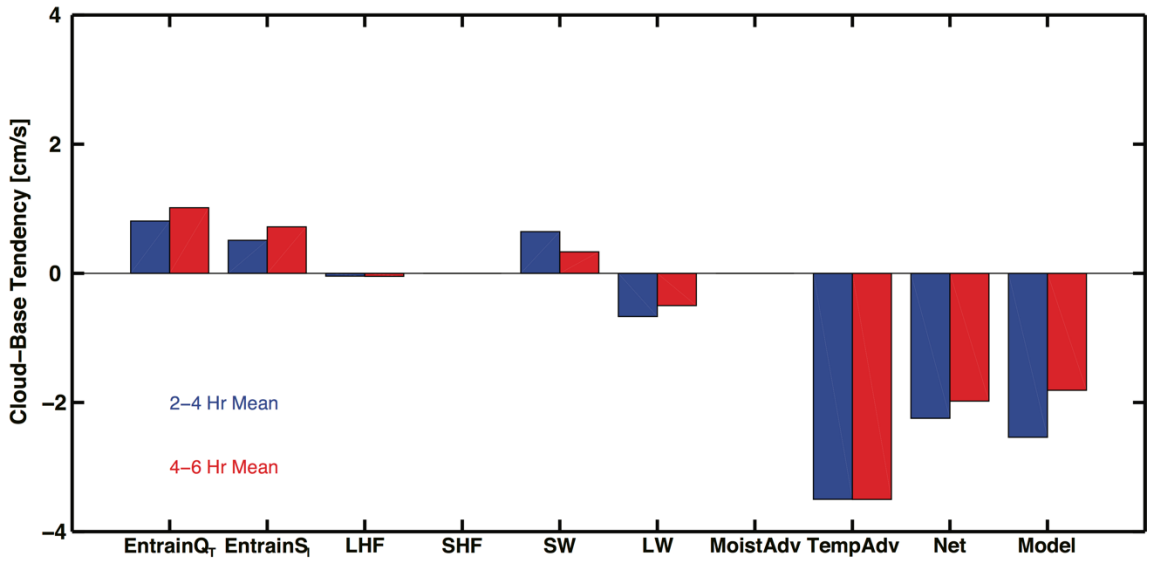

Fig. 22. Same as Fig. 18, but for a negative temperature tendency of 1 K hr^{-1}

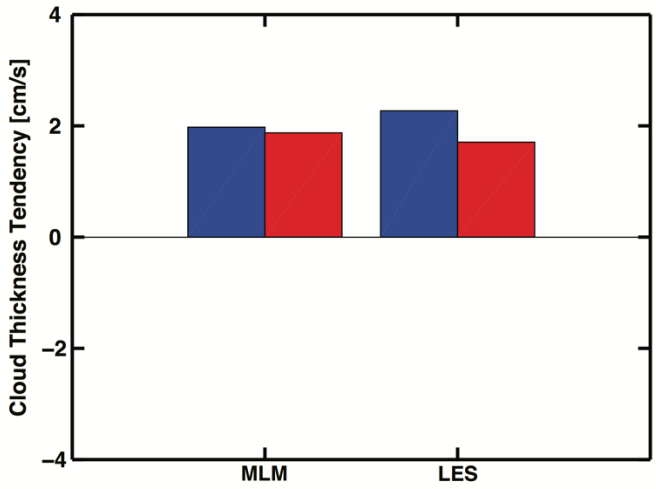

Fig. 23. Same as Fig. 19, but for a negative temperature tendency of 1 K hr^{-1}

c.) Surface Flux Budget Analysis

Surface flux sensitivity tests resulted in the largest q_T budget uncertainties of all the simulations, with 100% of the available analysis periods (5 2-hour periods) suffering from relative errors greater than 0.50 (Appendix C). There were also several significant errors in the MLM S_l budget tendencies, with absolute relative errors greater than 5.00 associated with overestimation of warming in the 2-4-hour period. The systematic overestimation of boundary-layer warming in the MLM implies that the depth of the entrainment layer is either deeper or that the entrainment flux at the interface occurs over a shallower depth of lower entrainment fluxes. Additionally, during the 2-4-hour period the negative q_T budget tendencies in the model were notably underestimated by the MLM, indicating that the physical processes governing the nature of the entrained air between q_T and S_l may be different. With budget errors imposing large errors on cloud-base tendency budget terms, a meaningful budget analysis of the surface flux sensitivity runs cannot be done.

d.) Shear Budget Analysis

The most substantial MLM S_l budget tendency errors were present in the shear sensitivity runs. The degree of boundary-layer warming was consistently overestimated, which we suspect is related to our entrainment flux calculation method. The sensitivity test with no shear evolved quite similarly to the control, but the lack of mechanical mixing near cloud-top did not sufficiently mix the entrainment fluxes in the layer from the inversion base to the S_l flux minimum, and the actual entrainment flux experienced by the boundary-layer was of a smaller magnitude and closer to the inversion base. The opposite is true for the directional wind shear case, where increased shear production of TKE significantly weakened and deepened the

inversion layer. The overestimation in the directional shear case presumably arises from a deeper entrainment layer than what is expected from our inversion base to S_l flux minimum method. Much like the surface flux sensitivity tests, the budget uncertainties and stratification preclude a consequential discussion on individual budget terms. However, the model budgets can provide useful information. The sensitivity run that induced positive horizontal vorticity near cloud-top cooled the boundary-layer in the 2-4-hour period, while the negative horizontal vorticity run warmed. This contrast can be explained by the increased longwave cooling in the positive horizontal vorticity case, which had higher liquid water content.

e.) Radiative Forcing (Longwave-only) Budget Analysis

The longwave-only simulations based on the Control and no-subsidence setups underestimated entrainment warming and drying in all averaging periods. The Control longwave-only simulation had small relative errors (< 0.2), while the no subsidence longwave only run substantially underestimated the warming contribution of S_l (relative errors: 0.91 and 0.56) (Appendix D). Boundary-layer drying is greatest during the 2-4-hour period, while boundary-layer cooling is greatest is the 4-6-hour period. The q_T entrainment fluxes are approximately 60-80% larger and S_l entrainment fluxes are 70-145% larger than the Control (Appendix E). Entrainment fluxes decrease appreciably from the first to the second analysis period (Table 2). This may partly be associated with weak stratification early in the period or more likely ascribed to increased inversion strength. Model cloud-base tendencies are very close to zero in the control longwave only simulation, and with negative inversion tendencies, results in cloud thinning. The no-subsidence longwave only run entrains more, but the growing boundary-layer produces positive cloud-thickness tendencies.

Table 2. Comparison of the Control longwave only (CONTROLLW) and no-subsidence longwave only (NOSUBLW) cloud-base tendency budget terms (all numbers in cm s^{-1})

CONTROLLW	$\mathbf{EntrainQ_T}$	$\mathbf{EntrainS_l}$	LHF	SW	LW	Net	Model
2-4 Hr	0.71	0.39	-0.044	0.0	-0.74	0.32	-0.10
4-6 Hr	0.46	0.25	-0.047	0.0	-0.77	-0.12	-0.05
NOSUBLW	$\mathbf{EntrainQ_T}$	$\mathbf{EntrainS_l}$	LHF	SW	LW	Net	Model
2-4 Hr	0.78	0.54	-0.040	0.0	-0.80	0.48	0.24
4-6 Hr	0.60	0.44	-0.040	0.0	-0.78	0.22	0.31

CHAPTER 4

Summary and Conclusions

This study aimed to determine the dominant mechanisms governing the evolution of thin afternoon marine stratocumulus through the application of mixed-layer theory on LES output. Aircraft observations obtained during the first research flight of the UPPEF field campaign were used to constrain and validate model behavior. The evaluation of individual physical mechanisms modulating cloud properties in a highly non-linear, turbulent boundary-layer flow is nearly intractable by analyzing LES output alone. We instead analyze the LES output in the framework of a mixed-layer model budget. In an effort to reduce complexity, budgets of q_T and S_l were partitioned into moisture and energy source/sink terms, as put forth by Caldwell et al. (2005). The budgets were extended further to incorporate the relationship between cloud-base tendency and changes in q_T and S_l budgets (Wood 2007; Ghonima et al. 2015). In doing so, attributing relative contributions of each source/sink term on boundary-layer moisture can be deduced. The thin cloud response to a wide range of environmental forcing scenarios was examined by running a multitude of sensitivity tests.

While the MLM approach is a viable method to attain our research goals, this particular case presents several challenges. The inversion associated with the thin cloud is rather diffuse, violating the zero-order cloud-top jump assumption traditionally assumed in mixed-layer theory. The standard flux-jump formulation for the entrainment flux closure typically used in MLMs is not appropriate for our more diffuse inversion structure and requires a different approach. We found the most robust method to be a layer average of explicitly resolved LES entrainment fluxes from the inversion base to the height of the minimum S_l flux. Error analysis of LES and MLM budgets suggests the method does not capture all of the physical processes that contribute

to varying depths of the entrainment layer, with systematic biases overestimating warming and drying during the 2-4-hour period and underestimating in the 4-6-hour period. Future work should emphasize uncertainties regarding entrainment layer depth and perhaps relate to more physically-based variables such as cloud-top gradients, net radiative flux divergence, liquid water content, and specific TKE characteristics near cloud-top. The entrainment flux calculations introduce the main source of uncertainties in the q_T and S_l budgets, but often do not translate to significant errors in cloud-base tendency, with the exception of surface flux and shear sensitivity runs. Additional research is also necessary for the possibility of separate entrainment layer depths for q_T and S_l. The main source of uncertainty in cloud-base tendency budgets can be accredited to boundary-layer stratification. However, by utilizing LES budget tendencies, the error contribution from stratification can be estimated and factored into the analysis, since the errors lead to a consistent overestimation of cloud-base height.

The Control simulation agreed reasonably well with the available observations of vertical velocity variance, liquid water content, and radiative fluxes. Over the course of the afternoon the Control run underwent gradual cloud thinning both in terms of cloud thickness and LWP. The development of boundary-layer-depth eddies during the latter half of the simulation effectively distributed sub-cloud moisture into the cloud-layer, and the boundary-layer was able to become well-mixed. Mixed-layer budget analysis suggests that the entrainment flux contributions to cloud-base rises are near comparable in magnitude in both analysis periods, despite increased longwave cooling in the 4-6-hour period. We hypothesize that this may be a result of isolated cumulus development in the 2-4-hour period associated with initial moisture stratification and increasing stability later in the afternoon. In this weak surface moisture flux case the only way to lower the cloud-base is through changing the saturation point via longwave cooling. The thin

cloud longwave cooling is large enough to overcome shortwave warming and entrainment of warm/dry free tropospheric air (especially evident in 4-6-hour period), which results in a lowering of the cloud-base, but the lowering inversion tendency remains larger than the cloud-base lowering, leading to gradual cloud thinning.

Subsidence velocity was found to scale linearly with liquid water content, and mean-BL TKE values were found to remain quite similar with weaker subsidence promoting increased stratification through disproportionately warming and drying the cloud layer with increased entrainment rates. The increased warm air entrainment, latent heating, and solar absorption all act to warm cloud-top temperatures which slightly increases longwave radiative flux divergence for weaker subsidence. Also, the increased liquid water content in weaker subsidence cases results in a higher infrared emissivity (stronger longwave cooling) (Chylek and Ramaswamy 1982), which combined with the warmer cloud-top temperatures promotes larger cloud-top entrainment fluxes. Mixed-layer budget analysis indicates that the increase in the depth of the boundary-layer in weaker subsidence simulations negates the increased net radiative flux divergence, resulting in an insensitivity between subsidence rate and radiative cooling effects on cloud-base tendency. The weaker subsidence runs entrain more and therefore they dry and warm during the early afternoon, but as time progresses and shortwave warming subsides this transitions to cooling.

Both moisture and temperature tendency simulations performed best of all the environmental forcings in terms of relative errors with model budgets. Positive moisture advection runs entrain much more than the control, but the constant addition of moisture is able to compensate for the decrease in saturation caused by entrainment. Entrainment fluxes of both q_T and S_l increase in time with increasing positive moisture tendencies. In all cases where

moisture was added, the associated increase of entrainment drying and warming was smaller than the prescribed moisture tendency. Negative temperature tendencies dried and cooled the boundary-layer, and also exhibited entrainment fluxes that increased in time. The significant cooling of the boundary-layer lowered the cloud-top temperatures and reduced the relative importance of longwave flux divergence on boundary-layer cooling. Cloud-thickness increased in the early analysis period, despite strong shortwave warming. The simulations with no shortwave radiation resulted in entrainment fluxes that were much larger than the control and decreased in time in response to a stronger inversion. The budget analysis of runs changing the degree of wind shear and surface flux sensitivity tests was not presented, due to large budget uncertainties in comparison with the model.

As shown here, the mixed-layer cloud-base tendency approach can be a useful tool to discern which terms are most responsible for changes in boundary-layer saturation, which may not be possible from examining LES output independently. Our main findings are summarized in the following points:

- Despite substantial solar fluxes during the afternoon, which are typically understood to suppress TKE production and reduce entrainment relative to a nocturnal cloud-topped boundary-layer, entrainment fluxes that warm and dry the cloud layer remain strongly active.
- The magnitude of the reduction in solar warming later in the afternoon in most of our simulations is larger than the changes in entrainment fluxes from early afternoon to later in the evening (either increases or decreases), causing a relative lowering of the cloud-base with respect to early afternoon and a recovery of the cloud. Although, in the case of

the control, the reduced entrainment fluxes lead to a faster lowering of the inversion base height and thinned the cloud.

- In the absence of significant surface or advective forcing, entrainment fluxes are the main mechanisms governing the overall sign of the cloud-base. All simulations suggest that the q_T entrainment flux contributes more toward the evolution of cloud-base height than the S_l flux. The dependence on entrainment fluxes arises from the insensitivity of net radiative flux divergence term for simulations with LWP in the 10-50 g m^{-2} range (Appendix E).
- Sensitivity experiments varying subsidence, large-scale temperature/moisture tendencies, surface fluxes, shear, and radiative forcing produced largely predictable outcomes, including confirmation of previous studies that investigated the relationship between LWP and subsidence.

The research presented here remains loosely observationally constrained, with a lack of level legs in or near the cloud-top and few full soundings to gather meaningful LWP estimates from the aircraft. Observational campaigns of the future may employ several techniques to provide valuable constraints to the LES. A considerable amount of flight time may be spent near cloud-top and in-cloud, gathering liquid water content and vertical velocity variances, as well as the possibility of utilizing a high-rate mass spectrometer to trace boundary-layer dimethyl sulfide, which would allow for an estimation of entrainment rate by implementing the methods of Faloona et al. (2005). A high-frequency cloud radar, such as the University of Wyoming Cloud Radar, could also be mounted on the aircraft, as was the case in DYCOMS-II, and when flown above the cloud layer the radar provides detailed representations of cloud mesoscale structure. The long level-legs near cloud-top would also provide information regarding radiative

processes with onboard pyranometers and pyrgeometers. Ideally, the aircraft could follow the mean flow by flying a saw-tooth pattern near cloud-top where forward motion averages to the mean flow speed to allow for a more direct temporal comparison between idealized Lagrangian model frameworks and aircraft observations.

APPENDIX

Appendix A

TKE Budget Analysis

TOTAL TKE = BUOY + SHEAR + ADV TRANS + PRESS TRANS – DISSIP

BUOY – buoyancy source/sink of TKE
SHEAR – mechanical source/sink of TKE
ADV TRANS – advection of TKE by mean flow
PRESS TRANS – transport of TKE by pressure perturbations
DISSIP – viscous dissipation of TKE

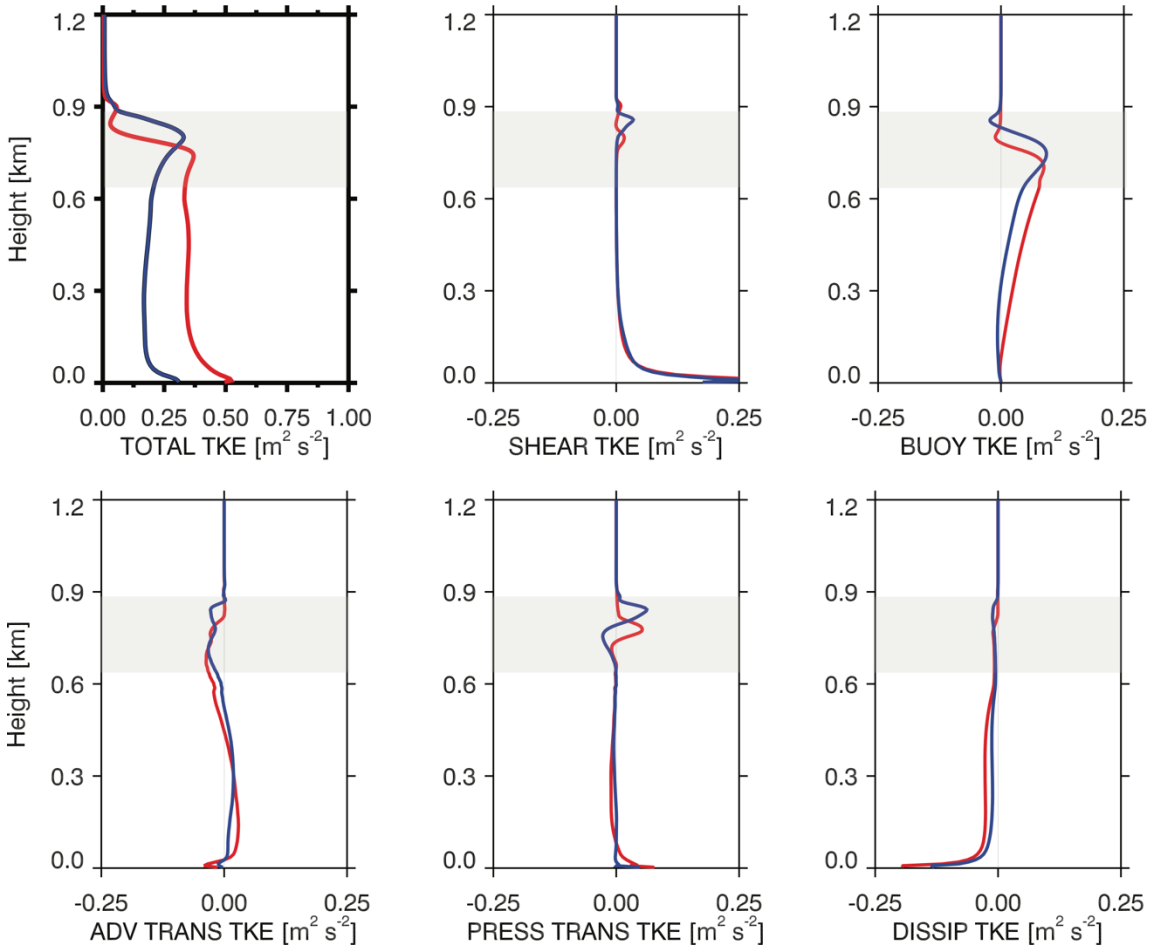

Appendix B

	Q_T Decoupling Parameter Value	S_l Decoupling Parameter Value
CONTROL 2-4 Hr Mean	0.039	0.014
4-6 Hr Mean	0.010	0.001
NOSUB 2-4 Hr Mean	0.048	0.021
4-6 Hr Mean	0.029	0.012
0.25 cm s^{-1} 2-4 Hr Mean	0.044	0.018
4-6 Hr Mean	0.018	0.008
0.5 cm s^{-1} 2-4 Hr Mean	0.043	0.018
4-6 Hr Mean	0.014	0.005
0.75 cm s^{-1} 2-4 Hr Mean	0.040	0.015
4-6 Hr Mean	0.011	0.003
1.25 cm s^{-1} 2-4 Hr Mean	0.039	0.013
4-6 Hr Mean	0.012	0.002
1.5 cm s^{-1} 2-4 Hr Mean	0.042	0.013
4-6 Hr Mean	0.039	0.032
MAA 0.25 2-4 Hr Mean	0.058	0.023
4-6 Hr Mean	0.048	0.016
MAA 0.5 2-4 Hr Mean	0.085	0.040
4-6 Hr Mean	0.013	0.062
MAA 1.0 2-4 Hr Mean	0.110	0.08
4-6 Hr Mean	0.130	0.11
DAA 0.25 2-4 Hr Mean	0.660	0.026
4-6 Hr Mean	--	--
CAA 0.25 2-4 Hr Mean	0.045	0.017
4-6 Hr Mean	0.013	0.005
CAA 1.0 2-4 Hr Mean	0.086	0.034
4-6 Hr Mean	0.093	0.038
CAA 2.0 2-4 Hr Mean	0.093	0.049
4-6 Hr Mean	0.048	0.026
WAA 1.0 2-4 Hr Mean	0.046	0.016
4-6 Hr Mean	--	--
LHF 100 2-4 Hr Mean	0.067	0.019
4-6 Hr Mean	0.021	0.009
LHF 150 2-4 Hr Mean	0.095	0.024
4-6 Hr Mean	0.084	0.031
SHF 100 2-4 Hr Mean	0.114	0.059
4-6 Hr Mean	--	--
NOSHEAR 2-4 Hr Mean	0.042	0.015
4-6 Hr Mean	0.019	0.004
Directional 2-4 Hr Mean	0.100	0.038
4-6 Hr Mean	--	--
PosVort 2-4 Hr Mean	0.050	0.019
4-6 Hr Mean	0.074	0.045
NegVort 2-4 Hr Mean	0.043	0.015
4-6 Hr Mean	0.013	0.001
ControlLW 2-4 Hr Mean	0.017	0.006
4-6 Hr Mean	0.006	0.000
NOSUBLW 2-4 Hr Mean	0.024	0.012
4-6 Hr Mean	0.010	0.004

Appendix C

	Model Q_T Tendency g kg^{-1} s^{-1}	MLM Q_T Tendency g kg^{-1} s^{-1}	Relative Error	Model S_l Tendency m^2 s^{-3}	MLM S_l Tendency m^2 s^{-3}	Relative Error
CONTROL 2-4 Hr Mean	-0.000011	-0.000016	0.45	-0.0028	-0.0018	-0.36
4-6 Hr Mean	-0.000012	-0.000011	-0.08	-0.0310	-0.0330	0.06
NOSUB 2-4 Hr Mean	-0.000019	-0.000022	0.16	0.0089	0.0059	-0.34
4-6 Hr Mean	-0.000020	-0.000019	-0.05	-0.0150	-0.0210	0.40
0.25 cm s^{-1} 2-4 Hr Mean	-0.000017	-0.000020	0.18	0.0057	0.0034	-0.40
4-6 Hr Mean	-0.000018	-0.000019	0.06	-0.0210	-0.0260	0.24
0.5 cm s^{-1} 2-4 Hr Mean	-0.000015	-0.000019	0.27	0.0028	0.0018	-0.36
4-6 Hr Mean	-0.000017	-0.000016	-0.06	-0.0260	-0.0300	0.15
0.75 cm s^{-1} 2-4 Hr Mean	-0.000014	-0.000018	0.29	0.0004	-0.0005	-2.36
4-6 Hr Mean	-0.000015	-0.000014	-0.07	-0.0300	-0.0340	0.13
1.25 cm s^{-1} 2-4 Hr Mean	-0.000008	-0.000014	0.75	-0.0043	-0.0020	-0.53
4-6 Hr Mean	-0.000007	-0.000006	0.14	-0.0220	-0.0230	0.05
1.5 cm s^{-1} 2-4 Hr Mean	-0.000005	-0.000009	0.80	-0.0024	0.0020	-1.84
4-6 Hr Mean	-0.000002	-0.000001	-0.50	0.0080	0.0110	0.38
MAA 0.25 2-4 Hr Mean	0.000041	0.000041	0.00	0.0150	0.0140	-0.07
4-6 Hr Mean	0.000036	0.000037	0.03	-0.0062	-0.0081	0.31
MAA 0.5 2-4 Hr Mean	0.000090	0.000100	0.11	0.0420	0.0290	-0.31
4-6 Hr Mean	0.000080	0.000084	0.08	0.0340	0.0240	-0.29
MAA 1.0 2-4 Hr Mean	0.000170	0.000180	0.06	0.1400	0.1130	-0.19
4-6 Hr Mean	0.000130	0.000150	0.15	0.1430	0.1100	-0.23
DAA 0.25 2-4 Hr Mean	-0.000070	-0.000070	0.00	0.0100	0.0150	0.50
4-6 Hr Mean	--	--	--	--	--	--
CAA 0.25 2-4 Hr Mean	-0.000018	-0.000022	0.22	-0.0560	-0.0640	0.14
4-6 Hr Mean	-0.000022	-0.000021	-0.05	-0.0800	-0.0920	0.15
CAA 1.0 2-4 Hr Mean	-0.000038	-0.000031	-0.18	-0.2290	-0.2420	0.06
4-6 Hr Mean	-0.000036	-0.000038	0.06	-0.2290	-0.2370	0.03
CAA 2.0 2-4 Hr Mean	-0.000051	-0.000044	-0.14	-0.4290	-0.4580	0.07
4-6 Hr Mean	-0.000089	-0.000036	-0.60	-0.3490	-0.4990	0.43
WAA 1.0 2-4 Hr Mean	-0.000015	-0.000008	4.30	0.0630	0.0740	0.17
4-6 Hr Mean	--	--	--	--	--	--
LHF 100 2-4 Hr Mean	0.000020	0.000030	0.50	0.0080	0.0110	0.38
4-6 Hr Mean	0.000010	0.000030	2.00	-0.0110	-0.0150	0.36
LHF 150 2-4 Hr Mean	0.000040	0.000061	0.53	0.0000	0.5200	0.00
4-6 Hr Mean	0.000025	-0.00005	-3.00	-0.0014	0.0069	-5.93
SHF 100 2-4 Hr Mean	0.000030	-0.00002	-1.67	0.0100	0.0100	0.00
4-6 Hr Mean	--	--	--	--	--	--
NOSHEAR 2-4 Hr Mean	-0.000011	-0.000016	0.45	0.0002	0.0025	11.5
4-6 Hr Mean	-0.000011	-0.000010	-0.09	-0.0210	-0.0230	0.10
Directional 2-4 Hr Mean	-0.000006	-0.000014	1.30	0.0070	0.0240	2.43
4-6 Hr Mean	--	--	--	--	--	--
PosVort 2-4 Hr Mean	-0.000010	-0.000015	0.50	0.0026	0.0080	2.10
4-6 Hr Mean	-0.000004	-0.000003	-0.15	-0.0020	0.0055	-3.75
NegVort 2-4 Hr Mean	-0.000009	-0.000014	0.56	-0.0027	-0.0019	-0.30
4-6 Hr Mean	-0.000010	-0.000012	0.20	-0.0260	-0.0270	0.04
ControlLW 2-4 Hr Mean	-0.000027	-0.000027	0.00	-0.0240	-0.0280	0.17
4-6 Hr Mean	-0.000020	-0.000016	-0.20	-0.040	-0.042	0.05
NOSUBLW 2-4 Hr Mean	-0.000032	-0.000030	-0.06	-0.011	-0.021	0.91
4-6 Hr Mean	-0.000027	-0.000022	-0.19	-0.018	-0.028	0.56

Appendix D

Control simulation cross-sections of liquid water content and vertical velocity

2.75 hours

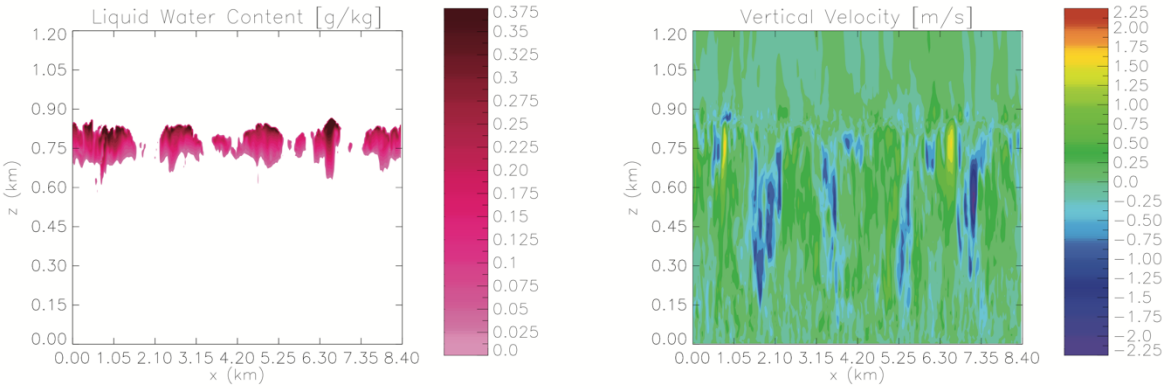

5.75 hours

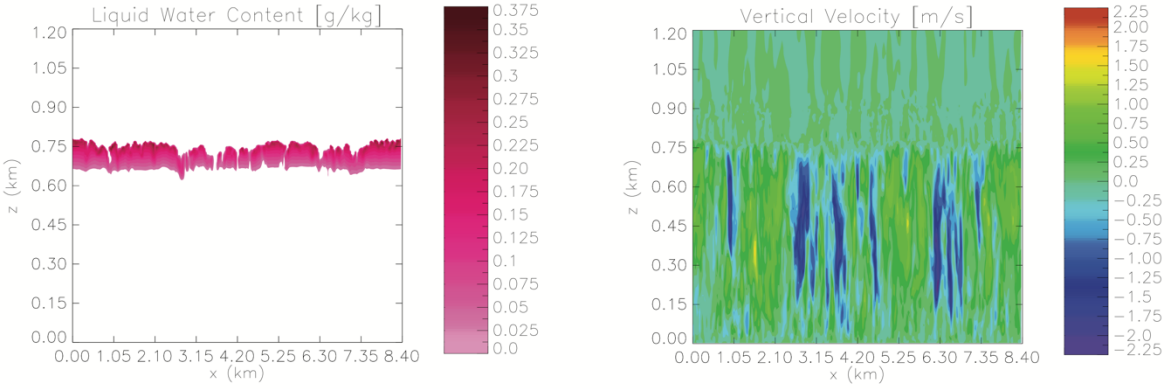

Appendix E

All terms in cm s^{-1}

	$EntrainQ_T$	$EntrainS_l$	LHF	SHF	SW	LW	MoistAdv	TempAdv	Net	Model
CONTROL 2-4 Hr Mean	0.44	0.22	-0.044	0.00	0.48	-0.73	0.00	0.00	0.37	-0.31
4-6 Hr Mean	0.34	0.17	-0.047	0.00	0.21	-0.80	0.00	0.00	-0.12	-0.25
NOSUB 2-4 Hr Mean	0.57	0.36	-0.041	0.00	0.52	-0.81	0.00	0.00	0.61	0.22
4-6 Hr Mean	0.53	0.35	-0.040	0.00	0.22	-0.82	0.00	0.00	0.23	-0.18
0.25 cm s^{-1} 2-4 Hr Mean	0.54	0.33	-0.042	0.00	0.51	-0.79	0.00	0.00	0.55	0.09
4-6 Hr Mean	0.51	0.31	-0.042	0.00	0.22	-0.85	0.00	0.00	0.14	-0.23
0.5 cm s^{-1} 2-4 Hr Mean	0.51	0.30	-0.042	0.00	0.50	-0.77	0.00	0.00	0.49	-0.03
4-6 Hr Mean	0.46	0.27	-0.044	0.00	0.21	-0.86	0.00	0.00	0.04	-0.27
0.75 cm s^{-1} 2-4 Hr Mean	0.49	0.27	-0.043	0.00	0.49	-0.77	0.00	0.00	0.44	-0.20
4-6 Hr Mean	0.41	0.22	-0.045	0.00	0.21	-0.86	0.00	0.00	-0.07	-0.22
1.25 cm s^{-1} 2-4 Hr Mean	0.39	0.17	-0.045	0.00	0.48	-0.68	0.00	0.00	0.32	-0.39
4-6 Hr Mean	0.20	0.09	-0.050	0.00	0.23	-0.61	0.00	0.00	-0.13	-0.23
1.5 cm s^{-1} 2-4 Hr Mean	0.29	0.12	-0.046	0.00	0.47	-0.56	0.00	0.00	0.27	-0.30
4-6 Hr Mean	0.04	0.02	-0.050	0.00	0.35	-0.23	0.00	0.00	0.12	-0.06
MAA 0.25 2-4 Hr Mean	0.70	0.40	-0.042	0.00	0.56	-0.78	-1.59	0.00	-0.75	-0.55
4-6 Hr Mean	0.78	0.45	-0.042	0.00	0.25	-0.80	-1.55	0.00	-0.91	-1.12
MAA 0.5 2-4 Hr Mean	0.89	0.59	-0.040	0.00	0.64	-0.87	-3.10	0.00	-1.85	-1.01
4-6 Hr Mean	1.22	0.87	-0.038	0.00	0.30	-0.88	-2.92	0.00	-1.45	-4.20
MAA 1.0 2-4 Hr Mean	2.06	1.42	-0.036	0.00	0.84	-0.85	-5.83	0.00	-2.40	-5.92
4-6 Hr Mean	2.55	1.68	-0.032	0.00	0.35	-0.69	-5.35	0.00	-1.50	1.76
DAA 0.25 2-4 Hr Mean	0.09	0.04	-0.045	0.00	0.49	-0.34	1.69	0.00	1.90	0.62
4-6 Hr Mean	--	--	--	--	--	--	--	--	--	--
CAA 0.25 2-4 Hr Mean	0.58	0.31	-0.044	0.00	0.51	-0.75	0.00	-0.87	-0.27	-0.51
4-6 Hr Mean	0.57	0.30	-0.047	0.00	0.23	-0.80	0.00	-0.87	-0.63	-0.68
CAA 1.0 2-4 Hr Mean	0.81	0.51	-0.044	0.00	0.65	-0.67	0.00	-3.50	-2.24	-2.54
4-6 Hr Mean	1.02	0.72	-0.047	0.00	0.33	-0.50	0.00	-3.50	-1.98	-1.81
CAA 2.0 2-4 Hr Mean	1.29	0.89	-0.044	0.00	0.93	-0.53	0.00	-7.00	-4.47	-5.07
4-6 Hr Mean	0.93	0.50	-0.047	0.00	0.40	-0.12	0.00	-7.00	-5.32	0.77
WAA 1.0 2-4 Hr Mean	0.25	0.12	-0.044	0.00	0.49	-0.57	0.00	0.87	1.10	0.10
4-6 Hr Mean	--	--	--	--	--	--	--	--	--	--
LHF 100 2-4 Hr Mean	0.62	0.34	-0.970	0.00	0.50	-0.71	0.00	0.00	-0.21	-0.76
4-6 Hr Mean	0.76	0.39	-1.000	0.00	0.23	-0.81	0.00	0.00	-0.43	-0.53
LHF 150 2-4 Hr Mean	0.58	0.33	-1.440	0.00	0.52	-0.76	0.00	0.00	-0.77	-2.30
4-6 Hr Mean	0.92	0.54	-1.480	0.00	0.24	-0.84	0.00	0.00	-0.62	0.77
SHF 100 2-4 Hr Mean	0.60	0.36	-0.042	1.28	0.54	-0.89	0.00	0.00	1.86	1.44
4-6 Hr Mean	--	--	--	--	--	--	--	--	--	--
NOSHEAR 2-4 Hr Mean	0.44	0.23	-0.044	0.00	0.48	-0.70	0.00	0.00	0.43	-0.24
4-6 Hr Mean	0.30	0.19	-0.048	0.00	0.22	-0.70	0.00	0.00	-0.03	-0.34
Directional 2-4 Hr Mean	0.40	0.32	-0.046	0.00	0.47	-0.48	0.00	0.00	0.65	-0.50
4-6 Hr Mean	--	--	--	--	--	--	--	--	--	--
PosVort 2-4 Hr Mean	0.43	0.26	-0.045	0.00	0.47	-0.63	0.00	0.00	0.48	-0.16
4-6 Hr Mean	0.15	0.12	-0.048	0.00	0.31	-0.36	0.00	0.00	0.17	0.09
NegVort 2-4 Hr Mean	0.40	0.20	-0.044	0.00	0.48	-0.71	0.00	0.00	0.34	-0.41
4-6 Hr Mean	0.35	0.19	-0.047	0.00	0.22	-0.75	0.00	0.00	-0.04	-0.24
ControlLW 2-4 Hr Mean	0.71	0.39	-0.044	0.00	0.00	-0.74	0.00	0.00	0.32	-0.10
4-6 Hr Mean	0.46	0.25	-0.047	0.00	0.00	-0.77	0.00	0.00	-0.12	-0.05
NOSUBLW 2-4 Hr Mean	0.78	0.54	-0.040	0.00	0.00	-0.80	0.00	0.00	0.48	0.24
4-6 Hr Mean	0.60	0.44	-0.040	0.00	0.00	-0.78	0.00	0.00	0.22	0.31

References

Ackerman, A., M. P. Kirkpatrick, D. E. Stevens, and O. B. Toon, 2004: The impact of humidity above stratiform clouds on indirect aerosol climate forcing, *Nature*, **432**, 1014–1017.

Albrecht, B. A., D. A. Randall, and S. Nicholls, 1988. Observations of marine stratocumulus clouds during FIRE. *Bull. Amer. Meteor. Soc.*, **69**(6), 618-626.

Bretherton, C. S., and M. C. Wyant, 1997: Moisture transport, lower-tropospheric stability, and decoupling of cloud-topped boundary layers. *J. Atmos. Sci*., **54**, 148–167.

Bretherton, C. S., P. N., Blossey, and J. Uchida, 2007: Cloud droplet sedimentation, entrainment efficiency, and subtropical stratocumulus albedo. *Geophys. Res. Lett*., **34**, doi:10.1029/2006GL027648

Burleyson, C. D., S. P. De Szoeke, S. E. Yuter, M. Wilbanks, and W. A. Brewer, W.A., 2013: Ship-based observations of the diurnal cycle of southeast Pacific marine stratocumulus clouds and precipitation. *J. Atmos. Sci.,* **70**, 3876-3894.

Burleyson, C.D. and S.E. Yuter, 2015: Patterns of Diurnal Marine Stratocumulus Cloud Fraction Variability. *J. Appl. Meteor. Climatol.,* **54**, 847–866

Caldwell, P., R. Wood, and C. S. Bretherton, 2005: Mixed-layer budget analysis of the diurnal cycle of entrainment in southeast Pacific stratocumulus. *J. Atmos. Sci*., **62**, 3775-3791.

Caldwell, P. and C. S. Bretherton, 2009: Large Eddy Simulation of the Diurnal Cycle in Southeast Pacific Stratocumulus. *J. Atmos. Sci*., **66**, 432-449.

Chen, T., W. B. Rossow, and Y. C. Zhang, 2000: Radiative effects of cloud-type variations. *J. Climate*, **13**, 264–286.

Chung, D., G. Matheou, and J. Teixeira, 2012: Steady-state large-eddy simulations to study the stratocumulus to shallow cumulus cloud transition. *J. Atmos. Sci.*, **69**, 3264-3276.

Chylek, P. and V. Ramaswamy, 1982: Simple Approximation for Infrared Emissivity of Water Clouds. *J. Atmos. Sci.*, **39**, 171-177.

Collins, W. D., and Coauthors, 2006: The Community Climate System Model Version 3 (CCSM3). *J. Climate*, **19**, 2122-2143.

Comstock, K., R. Wood, S. Yuter, and C.S. Bretherton, 2004: Radar observations of precipitation in and below stratocumulus clouds. *Quart. J. Roy. Meteor. Soc.,* **130**, 2891-2918.

Deardoff, J., 1980: Stratocumulus-capped mixed layers derived from a three-dimensional model. *Bound-Layer Meteor.*, **18**, 495-527.

de Roode, S. R., and P. G. Duynkerke, 1996: Dynamics of cumulus rising into stratocumulus as observed during the first 'Lagrangian' experiment of ASTEX. *Quart. J. Roy. Meteor. Soc.*, **122**, 1597–1623.

de Roode, S. R., I. Sandu, J. J. Van Der Dussen, A. S. Ackerman, P. Blossey, D. Jarecka, A. Lock, A. P. Siebesma, and B. Stevens, 2016. Large-Eddy Simulations of EUCLIPSE–GASS Lagrangian Stratocumulus-to-Cumulus Transitions: Mean State, Turbulence, and Decoupling. *J. Atmos. Sci.*, **73**(6), 2485-2508.

Faloona, I., D. H. Lenschow, T. Campos, B. Stevens, M. van Zanten, B. Blomquist, D. Thornton, A. Bandy, and H. Gerber, 2005: Observations of Entrainment in Eastern Pacific Marine Stratocumulus Using Three Conserved Scalars. *J. Atmos. Sci.*, **62**, 3268-3285.

Ghonima, M. S., J. R. Norris, T. Heus, and J. Kleissl, 2015: Reconciling and Validating the Cloud Thickness and Liquid Water Path Tendencies Proposed by R. Wood and JJ van der Dussen et al. *J. Atmos. Sci.*, **72**(5), 2033-2040.

Ghonima, M. S., T. Heus, J. R. Norris, and J. Kleissl, 2016: Factors Controlling Stratocumulus Cloud Lifetime over Coastal Land. *J. Atmos. Sci.,* **73**, 2961-2983.

Hartmann, D. L., and D. Short, 1980: On the use of earth radiation budget statistics for studies of clouds and climate. *J. Atmos. Sci.,* **37**, 1233–1250.

Hodur, R. M., 1997: The Naval Research Laboratory's Coupled Ocean/Atmosphere Mesoscale Prediction System (COAMPS). *Mon. Wea. Rev.*, **125**, 1414-1430.

Kessler, E., 1969: On the distribution and continuity of water substance in atmospheric circulations. *Meteor. Monogr.*, No. 32, Amer. Meteor. Soc., 84 pp.

Khairoutdinov, M.F., and D.A. Randall, 2003: Cloud resolving modeling of the ARM summer 1997 IOP: Model formulation, results, uncertainties, and sensitivities. *J. Atmos. Sci.*, **60**, 607-625.

Klein, S.A., and D. L. Hartmann, 1993: The seasonal cycle of low strati- form clouds. *J. Climate*, **6**, 1588–1606.

Lenschow, D. H., M. Zhou, Z. Zeng, L. Chen, and X. Xu, 2000: Measurements of fine-scale structure at the top of marine stratocumulus, *Bound.-Layer Meteor.*, **97**, 331–357.

Leon, D. C., Z. Wang, and D. Liu, 2008: Climatology of drizzle in marine boundary layer clouds based on 1 year of data from CloudSat and Cloud-Aerosol Lidar and Infrared Pathfinder Satellite Observations (CALIPSO). *J. Geophys. Res.,* **113**, D00A14, doi:10.1029/2008JD009835

Lewellen, D. C., and W. S. Lewellen, 1998: Large-eddy boundary layer entrainment. *J. Atmos. Sci.*, **55**, 2645-2665.

Moeng, C.-H., B. Stevens, and P. P. Sullivan, 2005: Where is the interface of stratocumulus-topped PBL? *J. Atmos. Sci.*, **62**, 2626–2631.

Monin, A.S., and Obukhov, A.M., 1954: Basic laws of turbulent mixing in the atmosphere near the ground. *Tr. Akad. Nauk SSSR Geofiz. Inst*, **24**(151), 163-187.

Myers, T. A., and J. Norris, 2013: Observational evidence that enhanced subsidence reduces subtropical marine boundary layer cloudiness. *J. Climate*, **26**, 7505–7524.

Nicholls, S., 1984: The dynamics of stratocumulus: Aircraft observations and comparisons with a mixed layer model. *Quart. J. Roy. Meteor. Soc.*, **110**, 783-820.

Nicholls, S. and J. Leighton, 1986. An observational study of the structure of stratiform cloud sheets: Part I. Structure. *Quart. J. Roy. Meteor. Soc.*, **112**, 431-460.

Noda, A. T., K. Nakamura, T. Iwasaki, and M. Satoh, 2013. A numerical study of a stratocumulus-topped boundary-layer: Relations of decaying clouds with a stability parameter across inversion. *J. Meteor. Soc. Japan. Ser. II*, **91**(6), 727-746.

Park, S., C. B. Leovy, and M. A. Rozendaal, 2004: A new heuristic Lagrangian marine boundary layer cloud model. *J. Atmos. Sci.,* **61**, 3002-3024.

Randall, D. A., 1980: Conditional instability of the first kind upside down. *J. Atmos. Sci*., **37**, 125–130.

Randall, D. A., J. A. Coakley Jr, D. H. Lenschow, C. W. Fairall, and R. A. Kropfli, 1984. Outlook for research on subtropical marine stratification clouds. *Bull. Amer. Meteor. Soc.,* **65**, 1290-1301.

Rozendaal, M. A., C. B. Leovy, and S. A. Klein, 1995: An observational study of the diurnal cycle of marine stratiform cloud. *J. Climate*, **8**, 1795-1809.

Sandu, I., J. L. Brenguier, O. Geoffroy, O. Thouron, and V. Masson, 2008. Aerosol impacts on the diurnal cycle of marine stratocumulus. *J. Atmos. Sci.*, **65**(8), pp.2705-2718.

Sandu, I., and B. Stevens, 2011. On the factors modulating the stratocumulus to cumulus transitions. *J. Atmos. Sci.*, **68**(9), 1865-1881.

Sears-Collins, A. L., D. M. Schultz, and R. H. Johns, 2006: Spatial and temporal variability of nonfreezing drizzle in the United States and Canada. *J. Climate*, **19**, 3629-3639; Corrigendum, 21, 1447-1448.

Stephens, G. L., 1978: Radiation profiles in extended water clouds: 1. Theory. *J. Atmos. Sci.*, **35**, 2111-2122.

Stevens, B., W. R. Cotton, G. Feingold, and C.-H. Moeng, 1998: Large-eddy simulations of strongly precipitating, shallow, stratocumulus-topped boundary layers. *J. Atmos. Sci.*, ***55***, 3616-3638.

Stevens, B., C. H. Moeng, and P. P. Sullivan, 1999: Large-eddy simulation of radiatively driven convection: Sensitivities to the representation of small scales. *J. Atmos. Sci.*, **56**, 3963-3984.

Stevens, B., and Coauthors, 2003: Dynamics and Chemistry of Marine Stratocumulus—DYCOMS II. *Bull. Amer. Meteor. Soc.,* **84**, 579–593.

Stevens, B., C. H. Moeng, A. S. Ackerman, C. S. Bretherton, A. Chlond, S. de Roode, J. Edwards, J. C. Golaz, H. Jiang, M. Khairoutdinov, and M.P. Kirkpatrick, 2005: Evaluation of large-eddy simulations via observations of nocturnal marine stratocumulus. *Mon. Wea. Rev.*, **133**, 1443-1462.

Turton, J. D., and S. Nicholls, 1987: Astudy of the diurnal variation of stratocumulus using a multiple mixed layer model. *Quart. J. Roy. Meteor. Soc.,* **113**, 969–1009.

Van der Dussen, J. J., S. R. de Roode, and A. P. Siebesma, 2016: How large-scale subsidence affects stratocumulus transitions. *Atmos. Chem. Phys*., **16**, 691-701.

VanZanten, M.C., P. Duynkerke, and J. Cuijpers, 1999: Entrainment Parameterization in Convective Boundary Layers. *J. Atmos. Sci*., **56**, 813-828.

Wang, Q., P. Tellado, D. Khelif, K. Nielsen, H. Jonsson, and A. Bucholtz, 2014: UPPEF flight summaries for CIRPAS Twin Otter measurements. http://met.nps.edu/~qwang/UPPEF/UPPEF_summary.pdf

Wang, S., J. C. Golaz, and Q. Wang, 2008: Effect of intense wind shear across the inversion on stratocumulus clouds. *Geophys. Res. Lett.,* **35**, L15814, doi:10.1029/2008GL033865.

Warren, S. G., C. J. Hahn, J. London, R. M. Chervin, and R. L. Jenne, 1986: Global distribution of total cloud cover and cloud types over land. NCAR Tech. Note NCAR/TN- 2731STR, National Center for Atmospheric Research, Boulder, CO, 29 pp. 1 200 maps.

Warren, S. G., C. J. Hahn, J. London, R. M. Chervin, and R. L. Jenne, 1988: Global distribution of total cloud cover and cloud types over ocean. NCAR Tech. Note NCAR/TN-3171STR, National Center for Atmospheric Research, Boulder, CO, 42 pp. 1 170 maps.

Wood, R., 2007: Cancellation of aerosol indirect effects in marine stratocumulus through cloud thinning. *J. Atmos. Sci.*, **64**, 2657-2669.

Wood, R., 2012: Stratocumulus clouds. *Mon. Wea. Rev.*, **140**, 2373-2423.

Yamaguchi, T., and D. A. Randall, 2008: Large-eddy simulation of evaporatively driven entrainment in cloud-topped mixed layers. *J. Atmos. Sci.,* **65**, 1481–1504.

Yamaguchi, T., D.A. Randall and M.F. Khairoutdinov, 2011: Cloud modeling tests of the ULTIMATE-MACHO scalar advection scheme. *Mon. Wea. Rev.*, **139**, 3248-3264.

Zhu, P., and Coauthors, 2005: Intercomparison and interpretation of single-column model simulations of a nocturnal stratocumulus topped marine boundary layer. *Mon. Wea. Rev.*, **133**, 2741–2758.